Studies of the Vortex Phase Diagram of the Type II Superconductors $YBa_2Cu_3O_7$ and 2H-$NbSe_2$

by

Emanuele Di Nicolò

Department of Physics & Astronomy
University of Southampton

A Thesis Submitted for the degree of
Master of Philosophy

January 2002

UNIVERSITY OF SOUTHAMPTON

ABSTRACT

FACULTY OF SCIENCE

PHYSICS

Master of Philosophy

STUDIES OF THE VORTEX PHASE DIAGRAM OF THE TYPE II SUPERCONDUCTORS $YBa_2Cu_3O_7$ AND 2H-$NbSe_2$

by Emanuele Di Nicolò

The work presented in this thesis is devoted to clarifying and understanding the phase diagram and the vortex-melting line of two type II superconductors: the fully oxidised $YBa_2Cu_3O_7$ and 2H-$NbSe_2$.

With regard to the high temperature superconductor $YBa_2Cu_3O_7$, magnetisation techniques were used in order to investigate the genesis of the peak-effect from the melting transition on three pure single crystals. A phase diagram was mapped, different vortex phases were demarcated and two multicritical points on the melting line $B_m(T)$ were identified. In particular, the unequivocal existence of the lower multicritical point was confirmed. This point of convergence of several boundary lines is located at low field (≈5.5T) and defines (together with the upper multicritical point) a region in which an ordered elastic solid melts in to a liquid via a first order transition. The intrinsic nature of this point was demonstrated and a possible explanation of its origin was given. The behaviour of the boundary lines, the shape of the phase diagram and the positions of both multicritical points reveal a pronounced and surprising symmetry.

The other system investigated in this thesis is the low temperature superconductor 2H-$NbSe_2$. Using a ^3He insert, DC transport measurements were performed down to 0.3 Kelvin. The resistance of the sample was measured as a function of the magnetic field (for fixed temperatures) and of the temperature (for fixed fields). From these measurements boundary lines and details of the melting transition were extracted. Combining this data with magnetic measurements performed on a similar sample, a complete description of the phase diagram was obtained. The irreversibility line extracted by the latter measurements almost coincides with the melting region obtained with transport techniques. Surprisingly, the melting line does not approach the upper critical field $B_{C2}(T)$ when reaching very low temperatures (0.3 Kelvin) as the theory predicts. Finally, one of the most interesting feature displayed by 2H-$NbSe_2$ is a fine structure revealed in the melting-process. In particular, a very narrow jump in the melting region is observed and a possible explanation is proposed.

CONTENTS

CHAPTER 1. INTRODUCTION 1

Acknowledgments

I consider the opportunity which I had to work for one year here at the department of Physics in Southampton a great privilege and it is a pleasure to thank all the people to whom I am indebted.

Firstly, I would like to thank my supervisor *Peter de Groot* for giving me the opportunity and the resources to conduct this study and also for his assistance during this year.

Special thanks are also due to the Research Fellows of our group *Sergey Gordeev* and *Alexander Zhukov* for their invaluable help in the experimental part of this work. The former is also acknowledged for the considerable assistance in the preparation of this document.

My gratitude goes also to *Nick Hinchcliffe* for his indispensable technical support in all the practical works. Thank you Nick also for your patience while you were teaching me.

Many thanks should go to *Jean Marc* first of all for being my friend. I really appreciated the time we had together and your support which continued after my permanence in Southampton. I hope to have the possibility to enjoy our friendship again in the future.

I am also indebted to a lot of other people which unfortunately I will hardly have the opportunity to meet again: in particular my housemates (among the others *Donald* and *Abdul*) and a number of italian guys which I met here in Southampton.

It would also be unfair to omit mentioning the contribution of people that, for all this year, have given their support to me while being in Italy. My gratitude goes to my family, my brother *Pierpaolo*, my uncle *Enrico* and some friends*: Marco, Samuele, Luigi, Matteo, Paolo.*

Chapter 1

Introduction

In 1911 Heike Kamerlingh Onnes [1] observed an abrupt loss of dc resistance of Mercury at a critical temperature T_c=4.2 K and gave the phenomenon the name of superconductivity. During the following decades many more metallic elements, compounds and alloys were found to become superconductive with increasingly higher transition temperatures up to 23 K.

In 1986 superconductivity was found in a completely new class of materials: the layered oxide compounds. This discovery quickly led to materials that are superconductive at 90 K and higher temperatures that enormously reduce the difficulty of cooling. These oxide materials were given the name "high temperature superconductors" (HTS). Instead the old superconductors are usually called "low temperature superconductors" (LTS). In general, materials that enter a superconductive state possess, in addition to zero dc resistance, tendency to exclude magnetic flux, a gap in the excitation energy spectrum, long range order of the electronic wave function and particular behaviour whenever they are coupled by weak links in superconductive junctions.

These features are now largely explained theoretically only for low temperature superconductors because there is no agreement regarding the microscopic mechanisms underlying superconductivity for HTS.

1.1 Superconductivity

Traditionally, there are two features that characterise the superconducting state below a certain critical temperature T_c. The first one is the above mentioned zero dc resistivity: a superconductor, when biased with a (not too large) direct current, does not produce a voltage, appearing as a perfect conductor. The second feature is the complete expulsion of the magnetic flux from the bulk of the specimen. More precisely, the magnetic field is screened from the inner part of the sample by currents flowing over the surface in a width of the order of 10^2 nanometers. There is virtually no current in the bulk of the material. This phenomenon is known as Meissner–Ochsenfeld effect [2] and cannot be explained simply by perfect conductivity because the expulsion takes place even when the magnetic field is applied before cooling the material below T_c. In fact in this case, a perfect conductor would tend to trap within the bulk the field applied in the normal state. It should also be noted that this phenomenon is observed over the entire frequency range from dc to optical frequencies.

In general, if a material can exist in a superconductive state only when the magnetic field is completely expelled from the bulk of the sample it is said to be a ***type I superconductor***.

The existence of this diamagnetism demonstrates that superconductivity is a true thermodynamic state and implies that a strong enough magnetic field H_c will destroy the superconducting state. This thermodynamic critical field $H_c(T)$ is approximately described by the following parabolic law, $H_c(T) \sim H_c(0)[1-(T/T_c)^2]$ as shown in Fig. 1.1. Using thermodynamic considerations it is possible to correlate this critical field with the superconducting condensation energy.

The first successful attempt to describe the electrodynamics properties of a type I superconductor is the London model proposed by the London brothers in 1935 [3]. They proposed two phenomenological equations which govern the microscopic electric and magnetic field in the superconductor. These equations are:

$$\Lambda \frac{\partial J}{\partial t} = \boldsymbol{E} \tag{1.1a}$$

$$\Lambda(\nabla\times\boldsymbol{J})+\boldsymbol{B}=0 \qquad (1.1b)$$

where $\Lambda = 1/\mu_0\lambda^2$.

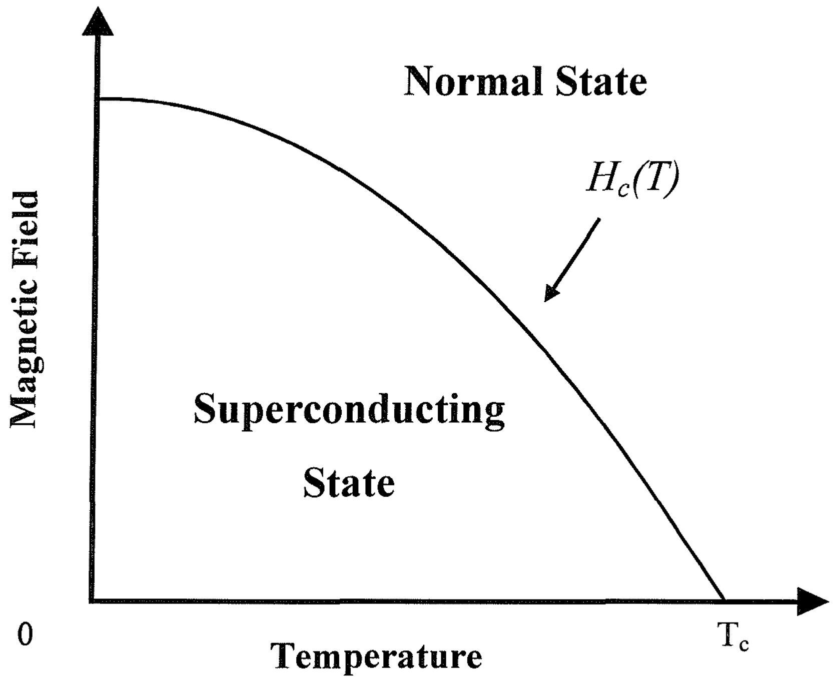

Fig. 1.1. Traditional phase diagram of a type-I superconductor, illustrating the dependence of the critical field H_C on T.

The first equation expresses the dependence of the electric field from the current: when the electric field is present, it controls only the time derivative of the current. This means that for stationary currents no electric field exists in any point of the superconductor. In contrast with the situation in a normal conductor, the second equation shows that it is the magnetic field (and not the electric field) that determines the current flowing in the superconductor. Using the second equation in conjunction with Maxwell's equations we obtain the exponential decay of both an external magnetic field and the corresponding induced current, i.e., the Meissner–Ochsenfeld effect. λ, which is called the penetration depth, is the distance required to fall to 1/e times the externally applied magnetic field. It is related to the density of the superconducting electrons and diverges as one approaches T_C.

The applicability of the London theory is limited by the fact that it cannot deal with strong magnetic inductions at the surface of the superconductor; furthermore the equations apply only for weak fields and they do not account for the disappearance of superconductivity in high magnetic fields.

A more general macroscopic theory was introduced by Ginzburg and Landau in 1950 [4]. Based on Landau's general theory of phase transitions this phenomenological model postulates the existence of an order parameter which can be used as a measure of the condensation in a superconductor. This order parameter is a complex quantity representing a macroscopic effective wave-function and can be written as:

$$\psi(\boldsymbol{r})=|\psi(\boldsymbol{r})|\exp\,[i\theta(\boldsymbol{r})] \qquad (1.2)$$

where $\theta(\boldsymbol{r})$ is the position-dependent phase and $|\psi(\boldsymbol{r})|$ can be interpreted as $[n_s(\boldsymbol{r})/2]^{1/2}$, $n_s(\boldsymbol{r})$ being the density of the superconducting electrons. After a minimisation procedure of the free energy of a superconducting body, the theory obtains two coupled non-linear differential equations describing the distribution of the magnetic induction and the order parameter in the equilibrium state. The important point is that the Ginzburg-Landau (GL) solutions of these equations can describe the way in which $|\psi(\boldsymbol{r})|$ (i.e. $n_s(\boldsymbol{r})$) changes in response to an applied magnetic field, giving details of the internal structure of the superconducting state and allowing the analysis of systems with physical properties spatially variable.

The GL theory also introduces a new length ξ which describes the scale of variation of the order parameter. The ratio λ/ξ = K is the GL parameter that is approximately temperature independent because both λ and ξ diverge as $(T_c\text{-}T)^{1/2}$ near T_c.

Just a few years later a physical explanation of the wave-function introduced by the GL theory was given by the Bardeen-Cooper-Schrieffer (BCS) microscopic model [5]. This theory is based on the hypothesis that in the superconducting state the electrons occupy $\boldsymbol{K}$ and spin states in pairs (Cooper pairs) and that there is a net attraction between members of the pairs due to electron-phonon interaction. In the superconducting ground state at T=0 all the electrons are paired and a certain amount of energy is required to break the pairs: this is the energy gap $\Delta(T)$ between the ground state and the quasi-particle excitations observed in experiments. From the BCS theory the London equations can be derived and subsequently in 1959 Gor'kov [6] demonstrated that GL theory is a limiting form of the BCS theory for temperatures near T_C and a not too fast spatial variations of $\boldsymbol{B}$.

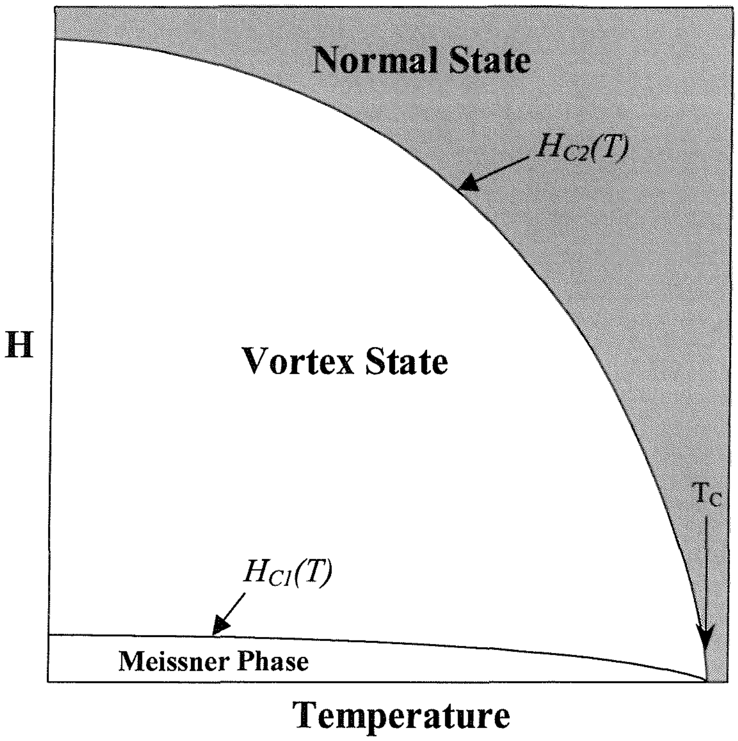

Fig. 1.2. magnetic field vs temperature phase diagram of a type II superconductor. The region between the $H_{c1}(T)$ and $H_{c2}(T)$ lines is the mixed state where the vortex matter exists.

At approximately the same time, Abrikosov [7] demonstrated theoretically the existence of a new class of superconductors in which the B-T phase diagram is similar to that showed in Fig. 1.2. For this class of materials the Ginzburg-Landau number $K>1/\sqrt{2}$. They were called type II to distinguish them from the type I for which $K<1/\sqrt{2}$. Type II superconductors are many LTS alloys and all known HTS. As we can see from Fig. 1.2, the existence of the Meissner phase is allowed only until a ***lower critical field*** $H_{C1}(T)$ then at higher fields is energetically more favourable for the material that the field penetrates homogeneously in the form of quantized flux lines called ***fluxons***. Each of this vortex line carries one quantum of magnetic flux $\Phi_0=h/2e\sim2.07\text{x}10^{-15}$ Wb [8] and consists of a normal core with diameter ξ in which the superconducting order parameter (i.e. the density of Cooper pairs) vanishes.

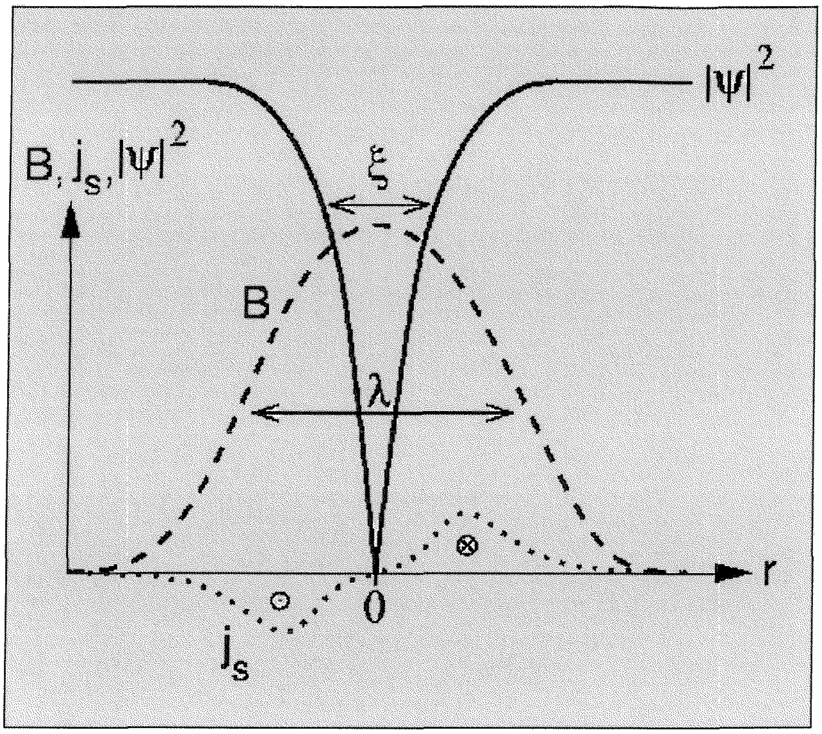

Fig. 1.3. Schematic representation of a vortex in a type II superconductor, showing the variation in the superconducting order parameter $|\psi|^2$ *and local magnetic induction B. Also indicated is the variation in the supercurrent density* (j_s) *around the vortex core.*

Fig. 1.3 shows the structure of an individual vortex: due to the circulating screening current made of Cooper pairs, the local magnetic induction falls off as $\exp(-r/\lambda)/\sqrt{r}$ (λ being the penetration depth) on moving away from the centre of the vortex. The regime comprised between $H_{C1}(T)$ and $H_{C2}(T)$ (***upper critical field***) is called "mixed state" or "Shubnikov phase" and ideally the vortex lines, repelling one another, form a regular triangular lattice with the nearest neighbour distance being

$$a_0 = (2/\sqrt{3})^{1/2}[\Phi_0/B]^{1/2} \qquad (1.3)$$

This means that the lattice spacing decreases continuously as the applied field increases from H_{C1} to H_{C2}. The existence of such a perfect triangular lattice has been confirmed in a number of elegant experiments since 1970s [9].

Up until the 1980s the record for the highest critical temperature of a superconductor was 23K in Nb_3Ge [10]. The discovery of high temperature superconductivity in cuprates by Bednorz and Muller in 1986 [11] gave a tremendous impulse to the research that quickly led to materials that are superconducting at temperatures above the temperature of the liquid nitrogen. Since then, in spite of the great progress obtained in fabricating new HTS materials and successful devices, the basic microscopic mechanism responsible for the high temperature superconductivity has not been still completely clarified. At this time there are numerous competing theory. It is generally believed that the pairing mechanism involves a d-wave symmetry and not a s-wave symmetry like the BCS theory predicts for conventional LTS. In addition, it is worth noting that in these new materials the mixed state shows a more complicated and richer behaviour than in the conventional type II. This is due in particular to the strongly layered structures and the significantly enhanced influence of thermal fluctuations that give raise to new phenomena that are accessible in experimental investigations [12].

1.2 Outline of thesis

The work presented in this thesis is directed to the understanding of the phase diagram of two different type II superconductors: the high T_C $YBa_2Cu_3O_{7-\delta}$ (in its fully oxidised state, i.e. $\delta=0$) and the low T_C 2H-$NbSe_2$. For this reason, the last part of this chapter is devoted to a brief description of the structures and main physical properties of these two superconductors. The rest of the thesis is organised as follows.

Chapter 2 represents a sort of theoretical background for the experimental results presented in the last two chapters. It describes, without any pretension to be exhaustive, the current knowledge of the equilibrium phase diagram. It starts by reviewing the basic properties characterising the wide class of type II superconductors. The successive part of the chapter is devoted to explaining the elastic properties of an ideal vortex lattice in the presence and absence of quenched disorder. The effects of thermal fluctuations are also considered in order to give a picture of the predicted vortex phase diagram. Subsequently the main properties of different kinds of vortex solid are discussed. Particular emphasis is given to the distinction between the so called Bragg-glass phase and other glassy phases.

In the first part of **Chapter 3** we explain and compare the two probing techniques of transport and magnetisation. In particular with regard to magnetic measurements, we describe the two methods of torque and vibrating sample magnetometer which have been used to study $YBa_2Cu_3O_7$ crystals. Subsequently there follows a detailed description of the ^3He system that has been used to carry out transport measurements. This system allowed us to study the superconductive properties of 2H-$NbSe_2$ down to 0.3 Kelvin. In the final part of the chapter we give details of the Grenoble High Field Transport Arrangement used to perform magnetisation experiments up to 28 Tesla.

Chapters 4 and **5** contains our experimental results.

In **Chapter 4** we show the magnetisation measurements performed on three pure single crystals of $YBa_2Cu_3O_7$ in order to investigate the genesis of the peak-effect from the melting transition. This allowed the phase diagram to be mapped, different vortex phases demarcated and two multicritical points identified on the melting line $B_M(T)$. In particular we confirmed the unequivocal existence of the lower multicritical point. This point of convergence of several boundary lines is located at low field (~5.5T) and defines (together with the upper multicritical point) the region in which an ordered elastic solid melts in to a liquid via a first order transition. The intrinsic nature of this point was demonstrated and an attempt to explain its origin was given. The behaviour of the boundary lines, the shape of the phase diagram and the positions of both multicritical points revealed a pronounced and surprising symmetry.

The other system investigated in this thesis is the low temperature superconductor 2H-$NbSe_2$. The results concerning this material are discussed in **Chapter 5**. Using a ^3He insert, we performed dc transport measurements down to 0.3 Kelvin. The resistance of the sample was measured as a function of the magnetic field (for fixed temperatures) and of the temperature (for fixed fields). From these measurements we extracted phase boundary lines and analysed details of the melting transition. Combining this data with magnetic measurements performed on a similar sample, a complete description of the phase diagram was given. The irreversibility line extracted by the latter measurements almost coincides with the melting region obtained with transport techniques. It is important to note that, in contrast to theoretical predictions, this melting region does not approach the upper critical field when reaching very low temperatures (0.3 Kelvin).

Finally, one of the most interesting features displayed by 2H-$NbSe_2$ is the fine structure revealed in the melting-process. In particular, a very narrow jump in the melting region was observed and a possible explanation was proposed.

In the **Main Conclusions** there is a review of the main findings arising from this thesis.

1.3 Structure and Properties of $YBa_2Cu_3O_{7-\delta}$ and 2H-$NbSe_2$

1.3.1 $YBa_2Cu_3O_{7-\delta}$ as a Member of the HTS Class

The oxide superconductors (like $La_{2-x}Sr_xCuO_4$, $YBa_2Cu_3O_{7-\delta}$, $Bi_2Sr_2CaCu_2O_8$, and $HgBa_2Ca_2Cu_3O_8$) have the so-called perovskite crystal structure. All the compounds possess a layered structure made of superconducting CuO_2 layers or sheets separated by insulating metallic oxide blocks of variable thickness. It is believed that these blocks can exert a sort of "chemical pressure" that confines charge carriers in the sheets. One of the most important consequences of this layered structure is a pronounced anisotropy. In particular the superconductive properties in the direction perpendicular to the CuO planes (c-direction) are very different from directions parallel to the planes (ab-plane). This anisotropy can be characterised by the ratio of the charge carrier effective masses:

$\gamma = (M_c/m_{ab})^{1/2}$. Anisotropies vary considerably between the different HTS materials: the maximum value is $\gamma \sim 100$ in $Bi_2Sr_2CaCu_2O_8$ [13] in comparison to only $\gamma \sim 8$ for optimally doped $YBa_2Cu_3O_{7-\delta}$ [14]. All of these cuprate materials require difficult and complex fabrication procedures [15].

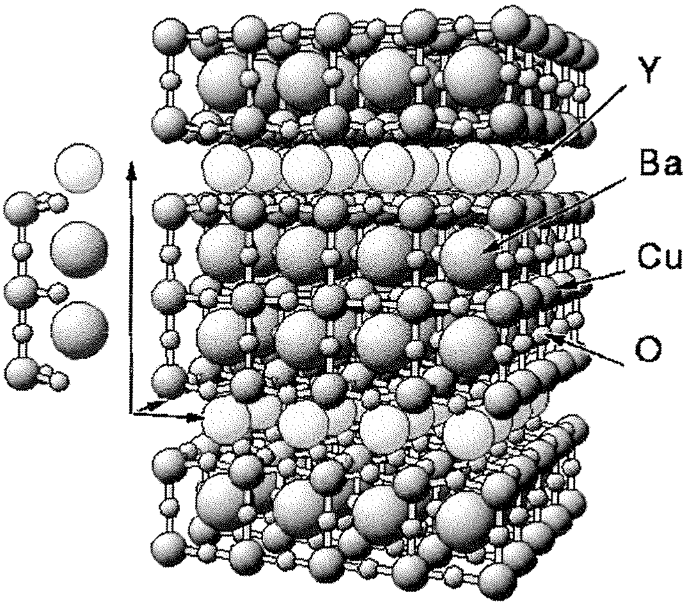

Fig. 1.4. Orthorhombic phase of $YBa_2Cu_3O_7$.

Soon after the discovery of HTS, most attention was focused on $YBa_2Cu_3O_{7-\delta}$ (often abbreviated to YBCO) a non-stochiometric compound with a transition temperature of about 93 K, whose structural and in particular superconductive properties vary considerably with its oxygen deficiency δ. In Fig. 1.4 it is shown in the fully oxygenated state (which is the case studied in this thesis in chapter 5) in which it displays an orthorhombic phase. For values of δ bigger than 0.65 this system becomes tetragonal and looses its superconductive properties [16]. But even in the orthorhombic phase, the properties of the system change considerably with oxygenation and this can be easily seen plotting the critical temperature T_c as a function of δ. This is done in Fig. 1.5 [16-17]. Note, in particular, the peak in T_c close to δ=0.07 and the sharp drop-off close to δ=0.6 which marks a transition from a superconducting orthorhombic phase to a tetragonal (anti-ferromagnetic) phase. Samples with oxygenation deficiency which give the highest Tc (grey region in Fig. 1.5) are termed as ***optimally doped.***

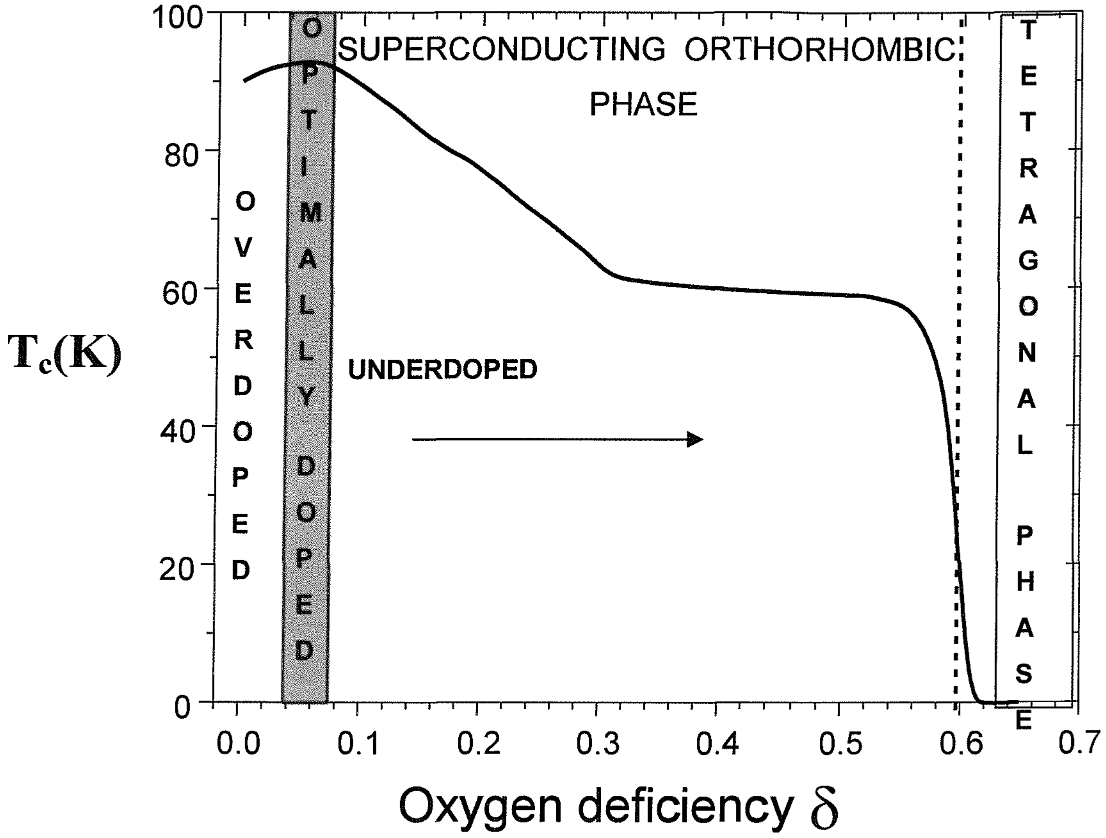

Fig. 1.5. Plot of the critical temperature of $YBa_2Cu_3O_{7-\delta}$ *single crystals as a function of the oxygen deficiency.*

Most of the studies on YBCO single crystals have been performed on these optimally doped samples; for this reason, the behaviour of the vortex system outside this region (***overdoped*** and ***underdoped*** cases) is poorly understood. Finally, it is also worth noting that oxygenation plays an important role in influencing the capacity of the system of capturing (***pinning***) the vortex lines present in the mixed state. This argument is discussed in chapter 2.

1.3.2 2H-NbSe$_2$ as a Member of the LTS Class

NbSe$_2$ belongs to the wide class of transition-metal dichalcogenides. It crystallises in layered structure of trigonal prismatic Se-Nb-Se slabs i. e. the anions (Se) are arranged as two parallel close packed sheets with the metal atoms occupying trigonal prismatic sites. The arrangement of the Niobium atoms with respect to each other is that of a closed-packed hexagonal layer. Depending on the growth conditions, NbSe$_2$ can have a packing sequence of either two layers (2H crystals) or four layers (4H crystals). A discussion of the two crystal structures and of other transition metal dichalcogenides is in the review article by Wilson and Yoffe [18]. Both two and four layer phases show a metallic behaviour over a wide temperature range and superconductivity at low temperatures [19-20]. In Fig. 1.6 it is shown a 3D view of the 2H phase.

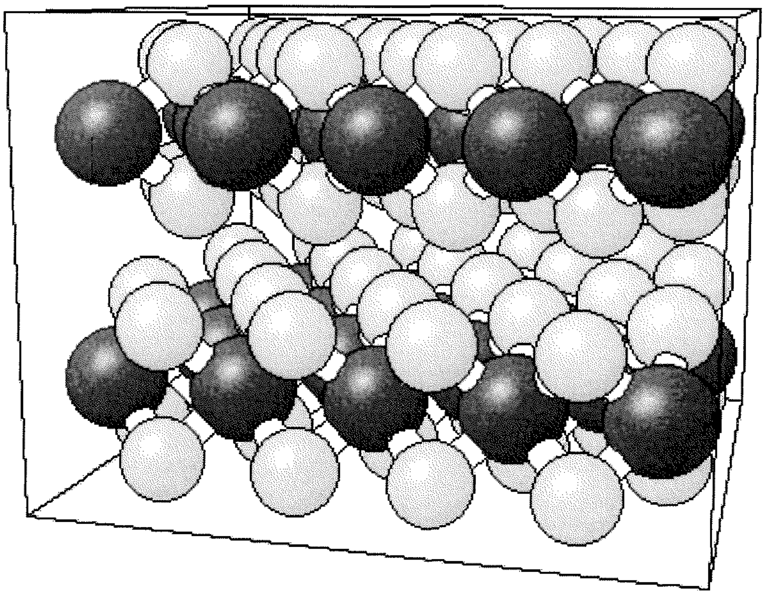

Fig. 1.6. 3D presentation of the crystal structure of 2H-NbSe$_2$.

The preparation techniques of 2H-$NbSe_2$ are well described in literature. One of the most used procedures is the chemical-transport method [20] in which the elements are allowed to react in evacuated silica tubes. This procedure gives large, homogeneous and well formed single crystals. Due to the crystal structure, this material has an anisotropy in its electronic properties of $\gamma \sim 3.3$ [21]. 2H-$NbSe_2$ has recently been studied due to its very weak capacity to pin the vortex lines, a property which makes it one of the cleanest single-crystals available if compared with its HTS cousins [22]. Note that the introduction of chemical impurities (in most of the cases Fe atoms from the preparation procedure) can produce the same effect that oxygen vacancies do in YBCO: enhancing the pinning properties of the material.

References

---

1 H. Kamerlingh Onnes, Leiden Comm. **120b**, **122b**, **124c** (1911).

2 W. Meissner and R. Ochsenfeld, Naturwissenschaften **21**, 787 (1933).

3 F. and H. London, Proc. Roy. Soc. (London) **A149**, 71 (1935).

4 V. L. Ginzburg and L. D. Landau, Zh. Experim. i Teor. Fiz. **20**, 1064 (1950).

5 J. Bardeen, L.N. Cooper and J.R. Schrieffer, Phys. Rev. **108**, 1175 (1957).

6 L. P. Gor'kov, Zh Eksperim. i Teor. Fiz. **36**, 1918 (1959) [JETP 9, 1364 (1959)].

7 A. A. Abrisokov, Zh Eksperim. i Teor. Fiz. **32**, 1442 (1957) [JETP 5, 1174 (1957)].

8 A. A. Abrisokov, Phys Chem. Solids **2**, 199 (1957).

9 H. Trauble and U. Essman, J. Appl. Phys. **39**, 4052 (1968).

10 J. R. Gavaler, Appl. Phys. Lett. **23**, 480 (1973).

11 J.G. Bednorz and K. A. Muller, Z. Phys. B **64**, 189 (1986).

12 G. Blatter et al., Rev. Mod. Phys. **66**, 1125 (1994).

13 D.E. Farrell et al., Phys. Rev. Lett. **63**, 782 (1990); J.C. Martinez et al., Phys. Rev. Lett. **69**, 2276 (1992).

14 D. E. Farrell et al., Phys. Rev. Lett. **64**, 1573 (1990).

15 M. B. Maple, J. Magnetism and Magn. Mater. **177-181,** 18 (1998).

16 J. D. Jorgensen, B. W. Veal et al., Phys. Rev. B **41,** 1863 (1990).

17 V. Breit et al., Phys. Rev. B **52,** R15 727 (1995).

18 J. A. Wilson and A. D. Yoffe, Advan. Phys. **18**, 193 (1969).

19 E. Revolinsky et al., J. Phys. Chem. Solids **26**, 1029 (1965).

20 R. Kershaw et al., Inorg. Chem. **6,** 1599 (1967).

21 P. de Trey et al., J. Low Temp. Phys **11,** 421 (1973).

22 M. J. Higgins et al., Physica C **257**, 232 (1996).

Chapter 2

The Vortex System and its Behaviour

In chapter 1 we briefly discussed the main differences between the two kinds of superconductivity. The aim of this chapter is to describe some of the most interesting features of the "vortex state" or "mixed state" of type II superconductors which actually is investigated in this thesis. Vortex-matter is certainly a very rich field both for theoretical and experimental research. It represents an interesting example of a condensed state with tunable parameters [18]. In fact, the density of the constituent particles (magnetic flux-lines) can be varied by several orders of magnitude simply by varying the external magnetic field. Furthermore vortex systems offer an alternative way of investigating disordered media.

A convenient and still useful phenomenological framework for type II superconductivity is the Ginzburg-Landau model. There are three important parameters that arise out the GL model:

I. ***Coherence length $\xi(T)$***: a length scale for variations in the superconducting wave-function as well as a range of the phase coherence in a Cooper pair.

II. ***Penetration depth $\lambda(T)$***: a length scale over which the magnetic field penetrates into the bulk of the superconductor.

III. ***Ginzburg-Landau parameter $\mathrm{K} = \lambda(T)/\xi(T)$***

In particular the GL parameter K is approximately temperature independent and controls the surface energy of the boundary between normal and superconducting regions. For $\mathrm{K} > 1/\sqrt{2}$ we have negative surface energies. This implies that it is energetically favourable to maximise the area of normal-superconducting boundaries in order to minimise the total free energy. The mixed state of a type II superconductor is threaded by vortex lines running in the direction of the applied magnetic field and arranged in a triangular or ***flux-line lattice*** (**FLL**). In the absence of defects and zero temperature these lines are straight and vortex-lattice demonstrates perfect ordering.

The lower critical field H_{C1} can be thought of as the field approximately necessary to produce one flux line in the material. The precise expression is:

$$H_{C1}=\Phi_0 \ln(\lambda/\xi)/(4\pi\lambda^2) \qquad (2.1)$$

As the external field is gradually increased, more and more flux lines enter into a specimen and the vortex distance decreases. At a certain point vortex-cores start to overlap and the whole sample becomes normal. This happens at

$$H_{C2}=\sqrt{2}\,\kappa H_C \qquad (2.2)$$

where H_C is the thermodynamic critical field $H_C=\Phi_0/(2\sqrt{2}\pi\lambda\xi)$. Both these two expressions for H_{C1} and H_{C2} can be easily obtained using the mean-field GL theory. But in a more realistic approach the thermal fluctuations have to be taken into account. For conventional LTS with high coherence lengths and low critical temperatures, the mean field model gives a good description of the behaviour around the transition, except for a very narrow region of about 10^{-4} K around T_C. Furthermore, the experimentally observed transition from a resistive phase for $T>T_C(H)$ to a zero-resistivity phase below $T_C(H)$ is very sharp. Instead HTS have short coherence lengths and high critical temperatures. For this reasons thermal fluctuations are much more important in a broad range around the $H_{C2}(T)$ line, the resistivity vanishes slowly and disappears completely only at a temperature lower than the mean field value $T_C(H)$.

2.1 Forces acting on Vortices

A wide range of different forces act on vortices present in a type II superconductor. Ideally, in a homogeneous material, a triangular lattice of vortices is formed. In practice, vortices are usually displaced from their ideal positions for several reasons. In particular, the exertion of pinning forces by inhomogeneities or structural defects in the sample, thermal fluctuations, gradients in the material parameters and finally, currents [1]. In the following paragraphs we will review the main interactions influencing the behaviour of a vortex system.

2.1.1 Vortex-Vortex interaction

We start by considering an ideal system with no impurities at zero temperature. In this case the interactions between flux lines threading a type II (isotropic) superconductor can be described by a two body potential between flux lines segments $\mathbf{dl_1}$ and $\mathbf{dl_2}$ separated by a distance r_{12} [2]:

$$U = \mathbf{dl_1}\,\mathbf{dl_2}\exp(-r_{12}/\lambda') - |\mathbf{dl_1}||\mathbf{dl_2}|\exp(-r_{12}/\xi') \qquad (2.3)$$

The first term reflects the long range force between circulating screening currents (repulsive for parallel flux lines) and the second term the short range attraction between the cores of the vortices. Here ξ' and λ' express the effective field-dependent penetration depth and coherence length respectively ($\lambda' = \lambda/\sqrt{1-b}$; $\xi' = \xi/\sqrt{1-b}$; $b=B/B_{C2}$). In the case of anisotropic superconductors it is important to consider the orientation of $\mathbf{r}_{12}$ with respect to the symmetry axis of the material but the interaction is of the same nature. The vortex-vortex interaction is responsible for the elastic rigidity of the vortex lattice. The elastic properties are described by a set of elastic moduli: the modulus for uniaxial compression C_{11}, the tilt modulus C_{44} and the shear modulus C_{66}. C_{11} reflects the rigidity of the flux line lattice against compression, C_{44} is a measure of the ease with which vortices can be tilted away from the magnetic field and C_{66} describes the resistance of the vortex lattice against shearing. These parameters can be calculated for isotropic and anisotropic superconductors [3] and are field dependent. In fact $C_{11}\sim C_{44}\sim b^2$ and $C_{66}\sim b(1-b)^2$.

2.1.2 Lorentz force induced by a transport current

In the same way in which a screening current resulting from a vortex distribution exerts a force on individual vortices, an imposed external current J produces a Lorentz force per unit length

$$f_L = \Phi_0(\boldsymbol{J} \wedge \boldsymbol{n}) \qquad (2.4)$$

that acts on vortices pushing them in direction perpendicular to the current and perpendicular to the orientation of the magnetic field (Fig. 2.1). Here $\boldsymbol{n}$ is a vector of unit length along which the vortex is directed. In a perfectly homogeneous system the Lorentz force is counteracted only by a friction force $\boldsymbol{F}_\eta = -\eta \boldsymbol{v}$, where $\boldsymbol{v}$ is the steady state velocity of the vortices, $\boldsymbol{v} = \boldsymbol{J} \wedge \boldsymbol{B}/\eta$. Thus, an electric field leading to a voltage and a corresponding

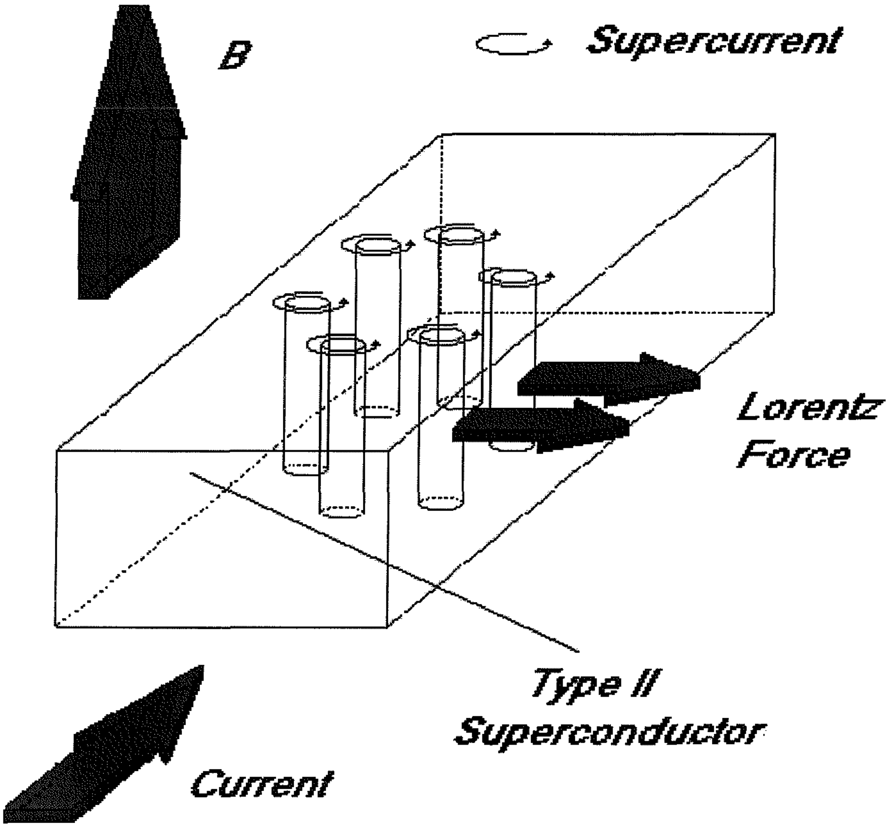

Fig. 2.1. When a current (arrow) is applied to a type II superconductor in the mixed state, the magnetic vortices (cylinders) feel the Lorentz force that pushes them at right angles to the current flow. This movement dissipates energy and produces resistance. Note that here it is considered the simplest case: B ⊥ layers and to the applied current.

dissipation of energy is generated by the flux motion in a manner analogous to Faraday's law of induction. This means that in absence of a force that prevents the dissipative flux motion there will always be a finite resistance. In the simple case in which $\boldsymbol{J}\perp\boldsymbol{B}$ the ***flux flow resistivity*** is approximately given by [4]:

$$\rho_{ff} \approx \Phi_0 B/\eta \tag{2.5}$$

The friction coefficient η can be obtained considering the dissipation processes inside and around the vortex cores [5], $\eta \approx \Phi_0 B_{C2}/\rho_n$ with ρ_n being the normal resistivity of the material. Substituting this expression in eq. (2.5) we see that, as observed in several experiments [6], the dissipation is just reduced by a factor B/B_{c2} as compared to the normal state. For this reason, in order to recover the property of dissipation-free current flow it is necessary to counteract the Lorentz force with a pinning force $\boldsymbol{F}_P$ to obtain $\boldsymbol{v}=0$ ($\boldsymbol{F}_L=0$).

2.1.3 Vortex-Pinning interaction

Any kind of inhomogeneities in a superconducting material can lead to a local suppression of the superconducting order parameter producing a finite pinning force that attracts a flux line to the inhomogeneity itself. In fact, in order to minimise the suppression of the order parameter each vortex tends to occupy the position of this imperfection, thereby only depleting the order parameter once (Fig. 2.2). For currents below a critical current density $J_C=F_P/B$ (assuming $\boldsymbol{J}\perp\boldsymbol{B}$) vortices are pinned and do not respond to a small enough applied Lorentz force. This means that the presence of pinning centres is a crucial factor for obtaining a dissipation-free current flow in a superconductor. It is important to note that J_C is always smaller than the depairing current density $J_0 \approx H_C/\lambda$ determined by the thermodynamic critical field H_C. The ratio J_C/J_0 is a measure of the pinning force density F_P and is a fundamental parameter in characterising type II superconductors. The presence of pinning sites (sometimes called "quenched disorder") affects the dynamical behaviour of vortices and destroys the positional order of the flux lattice by stimulating transverse wandering of the vortex lines.

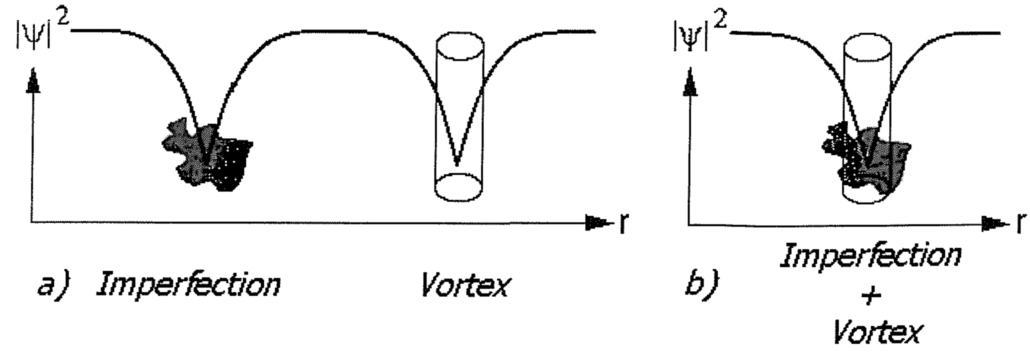

Fig. 2.2. a) Schematic plot of the density of Cooper pairs near an imperfection and a vortex line. b) When the vortex is placed into the imperfection the energy of the system is reduced [from Ref. 4].

The problem of calculating the pinning force produced by a random arrangement of ***weak*** pinning centres was first solved by Larkin and Ovchinnikov within their collective pinning theory [7]. The most essential idea of their analysis is coupling correlated volumes within the vortex lattice with the potential landscape induced by the pinning centres across those volumes. Each single vortex-line of length L_C (called the ***collective pinning length***) is characterised by a finite elasticity such that it can accommodate in the pinning potential and is pinned independently from the others. L_C can be calculated minimising the free energy of the vortex with respect to the length L over which the pinning forces add up randomly

$$L_C \cong [\varepsilon_0^2 \xi^2/\gamma]^{1/3} \qquad (2.6)$$

where γ is the variance of the strength of point disorder and $\varepsilon_0=[\Phi_0/4\pi\lambda]^2$ determines the self-energy of vortex lines and their mutual interactions. The resulting collective pinning energy is

$$U_C \cong H_C^2 \xi^2 [\xi/L_C] \qquad (2.7)$$

This energy is produced by the collective action of all the defects within the volume $V_C = \xi^2 L_C$. Balancing the Lorentz force against the pinning force acting on the individual segment allows a finite critical current density to be obtained

$$J_C \cong J_0[\xi/L_C]^2 \qquad (2.8)$$

The regime of weak collective pinning is characterised by a small critical current density J_C with respect to the depairing current J_0, $J_C \ll J_0$. From (2.8) we see that this means $L_C \gg \xi$. It is worth noting that the special properties of high T_C superconductors tend to render pinning in bulk material very weak (small J_C/J_0). This is due to the small coherence lengths and to the absence of extended pinning sites occurring in conventional superconductors.

It is also interesting to note that the shear modulus C_{66} of the FLL vanishes at the upper critical field producing a softening of the flux lattice and thereby a more effective pinning close to $H_{C2}(T)$: in fact a soft lattice should pin strongly than a more rigid one. This phenomenon (present both in HTS and LTS) is known as the ***peak effect*** [8] and experimentally manifests itself as an enhancement of the critical current.

There are different kinds of pinning objects in HTS such as $YBa_2Cu_3O_{7-\delta}$ (YBCO). The most important is the presence of oxygen vacancies that locally suppress the superconducting order parameter and are spatially uncorrelated. This fact was predicted for the first time by Tinkham [9] and recently it has been demonstrated that oxygen vacancies are the most important source of pinning in pure single crystals of YBCO [10].

Other important sources of pinning are extended defects like twin–plane boundaries and dislocations. They interact essentially in the same way with flux lines but since the defects are spatially extended the total pinning force can be considerably larger. Furthermore the pinning effect varies with orientation of the applied magnetic field relative to the defect [11]. Since it is very important for technological purposes to increase the critical current and optimise pinning, in recent years various methods have been introduced to increase disorder, such as electron irradiation, which produces uncorrelated point disorder, or heavy ion irradiation that creates parallel columns of defects (columnar disorder). In particular the columnar defects have been found to be very efficient to pin vortex lines [12].

2.1.4 Thermal interaction

The presence of thermal fluctuations in the phenomenology of type II superconductors affects both the phase diagram of the vortex system and its dynamical properties. It is useful to consider thermal interactions as a random shaking force upon the vortices. The mean-square amplitude of the shaking motion is related to the temperature via the expression: $\langle u^2 \rangle \propto T$, where the constant of proportionality is determined by the elastic moduli of the flux line lattice. The melting transition can be understood in terms of large thermal fluctuations in the position of the vortex lines. Using the phenomenological Lindemann melting criterion (that is known to work for ordinary crystals) the vortex lattice melts when the energy of thermal fluctuations becomes equal to the elastic barriers that keep vortices near their equilibrium position in the lattice [18].

The curve $B_m(T)$ in the T-H phase diagram at which the vortex lattice melts is called the melting line. Above this line we have a liquid, i.e. a phase that has lost its rigidity and is unable to support any shear ($C_{66}=0$). In principle the flux system should be a “liquid” even for fields very close to H_{C1} since the flux lines are separated by a distance larger than the interaction length λ, however in practice flux lines enter very rapidly in the specimen and this region in the phase diagram is experimentally hardly accessible. Nevertheless this melting effect has been observed experimentally in the low temperature superconductor $NbSe_2$ [13-14]. In HTS such as $YBa_2Cu_3O_{7-\delta}$ it is still an open question whether or not it is possible to observe the so called re-entrant melting line.

The presence of thermal fluctuations has at least two other important consequences in the dynamical behaviour of the vortex system:

I. ***Flux Creep*** [15-16]: thermal energy can induce vortex lines’ movement over the pinning barriers via thermally activated jumps even at current densities below J_C. This effect produces a small but finite motion of the vortices re-establishing dissipation in type II superconductors. This phenomenon is particularly evident in HTS where some flux motion (*giant flux creep*) occurs even at very low values of the current density [17].

II. ***Thermal depinning*** [18]: thermal fluctuations give raise to a smoothing of the quenched pinning potential and thereby reduce the critical current density J_C.

The fundamental parameter characterising the importance of thermal fluctuations in type II superconductors is the Ginzburg number [18]

$$Gi = \left[\frac{T_C}{H_C^2(0)\varepsilon\xi^3(0)}\right]^2 \Big/ 2 \tag{2.9}$$

Here $\varepsilon=(m/M)^{1/2}$ represents the mass anisotropy ratio [19]. For example, the Ginzburg parameter appears in the expression that defines the width of the critical regime or also in the function describing the shape of the melting line. Due to their short coherence lengths and high critical temperatures, HTS have much larger Ginzburg numbers (roughly six order of magnitude) than conventional low superconductors. This means that for HTS the critical fluctuations region and the part of the phase diagram where the vortex-lattice is melted are bigger. This also explains why the mean field description is no longer valid for this new class of materials. Furthermore HTS materials have an inherently layered structure consisting of CuO_2 planes separated by varying blocks of heavy elements. This fact produces a strong anisotropy that varies from moderate values as in YBCO ($\gamma = 1/\varepsilon \approx 10$) to very high values as in $Bi_2Sr_2CaCu_2O_8$ ($\gamma = 1/\varepsilon \approx 100$). Anisotropy strongly promotes thermal fluctuations since from (2.9) we see that $Gi \propto 1/\varepsilon^2$.

2.2 Vortex-Glass Scenario

Before the current interest for high Tc materials, the dynamics and the static of superconductors were treated in an oversimplified way and only after the discovery of the HTS the inadequacies of the conventional theory became clear. For the dynamics, the two main classes of experiments *(a)* transport (the form of the I-V characteristics) and *(b)* magnetisation relaxation experiments (relaxation of the magnetic field inside a sample due to the above mentioned flux creep) were considered in the framework of the conventional Anderson-Kim model. In this model a piece of vortex lattice (a vortex bundle) moves as a single particle in a one dimensional potential energy landscape. At T=0 we obtain a critical force F_C and at T>0 thermal energy allows motion of the flux lines by overcoming a barrier U_b and therefore producing an average velocity

$$v \sim \rho_{ff} F \exp[-U_b/T] \qquad (2.10)$$

where v is obviously proportional to the voltage drop V and F is the applied force (proportional to the current J). This mechanism (named ***TAFF**: **thermally assisted flux flow***) gives rise to an exponentially small but finite resistivity (i.e. vortex mobility) and therefore the mixed phase is not a true superconductive state at any finite temperature.

The TAFF model is completely insufficient in describing high T_C materials where giant thermal flux creeps were soon observed. For this reason the TAFF law was replaced by

$$v \sim \rho_{ff} F \exp[-U_b(J)/T] \tag{2.11}$$

with a barrier $U_b(J)$ that, in this case, exhibits a strong dependence on the current.

Regarding the static, it was soon observed the crucial role of the disorder and the remarkable difference of the phase diagram from the mean field one (shown in Fig. 1.3 chapter 1). In fact, in high Tc materials due to their higher anisotropy and temperatures, the vortex lattice melts on a line $H_M(T)$ which lies well below $H_{C2}(T)$ as predicted long before the advent of HTS [20]. In addition, it is present an irreversibility line $H_{irr}(T)$ [21], below which the system possesses a glassy behaviour with non linear I-V characteristics, vanishingly small linear resistivity and irreversibility. Furthermore it has been confirmed by a variety of techniques that the transition at low field and weak disorder is a ***first order*** transition [22-23-24].

All these facts suggested that the point like disorder may lead to the formation of a glassy state rather than that of a vortex lattice.

Basically, there are two ways of describing this glassy phase.

The first was introduced by Fisher [25] soon after the discovery of HTS materials. In this approach the pinning potential is incorporated from the beginning and not treated as a perturbation of a pure system. The basic assumption of this model is that both translational and topological order are completely destroyed by the presence of pinning disorder. The model introduces the concept of glassiness that was already well known from the study of spin-glass systems where magnetic impurities are randomly disposed on the sites of a regular translationally invariant lattice. In such systems, the corresponding random contribution in the coupling term between adjacent spins produces a wide range of characteristic phenomena such as irreversibility and metastability [26].

The ***vortex glass*** theory [25-27] (also named "gauge glass model") postulates that the presence of quenched disorder into the vortex system can give raise to a glassy state in some ways analogous to that observed in spin glasses. This glassy state is characterised by infinite pinning energy barriers leading to a strictly zero linear flux-flow resistance as J approaches zero, i.e. $\rho(J \rightarrow 0) \rightarrow 0$.

Obviously this happens below the melting line $B_m(T)$ where the shear modulus C_{66} of the vortex system becomes finite and thereby the response of the specimen to an external vanishing current density remains sub-Ohmic. The expression for the energy barriers to flux motion is:

$$E(J) \propto \exp[(-Uc/KT)(Jc/J)^{\mu}] \tag{2.12}$$

Here μ is a scaling exponent that is less than one for $T<Tg$. Furthermore the vortex-glass model predicts a continuos transitions in passing from a liquid to a glassy state.

The second approach [28] is completely different and describes vortex lines as strings having some elastic energy. In this case the vortex problem is treated as a particular case of the more general problem of an elastic system in the presence of disorder. Besides applying to vortex lattices, the elastic theory describes many other physical systems such as charge density waves, Wigner crystals, magnetic bubbles and Josephson junctions. All these systems have a perfectly ordered structure perturbed by elastic distortions and topological defects such as dislocations. This theory also agrees that disorder produces a vanishing linear resistivity and a glassy low temperature phase destroying the perfect Abrikosov lattice (existing in the mean field theory) at large scales.

Although different in nature both of the theories, therefore, predict a low temperature topologically disordered phase characterised by the absence of translational order. This phase should possess dislocations even at very low fields and temperatures.

These two approaches seemed to explain some aspects of the problem but many others remained unsolved. One of these is the above mentioned type of the transition between the glass and the liquid phase at low fields that is first order and not continuos as predicted by the gauge glass model. The other fact is certainly the observation, in decoration experiments of the flux lattice, that there are large regions free of dislocations at very low fields (≈60 G) in several superconductors [29]. This experimental result is completely inconsistent with the assumption behind the concept of vortex glass.

2.3 Bragg-Glass and Other Glassy Phases

In a number of recent theoretical publications [30-31-32] Giamarchi and Le Doussal (GLeD) have attempted to solve all these contradictions arising out both of the theories described in the previous paragraph. Their approach is based on the elastic model and predicts the existence of a new vortex-solid phase with perfect topological order and nearly perfect translational order, i.e. a ***quasi long range ordered phase***. In particular, GLeD by demonstrating that the wandering exponent ζ of flux lines falls to zero over large length scales, found that the effects of impurities on the translational order of the lattice is weaker than was previously thought and that quasi-long range order persists at large scales. This resulting phase has the property of being both a glass and quasi ordered (without dislocations).

In this new approach the system is modelled by stacks of coupled planes and described by layers of two dimensional triangular lattices of vortices. The expression for the total energy is[1]:

$$H=\frac{1}{2}\int d^2r dz[(C_{11}-C_{66})(\partial_\alpha u_\alpha)^2+C_{66}(\partial_\alpha u_\beta)^2+C_{44}(\partial_z u_\alpha)^2]+\int d^2r dz\, V(\boldsymbol{r},z)\rho(\boldsymbol{r},z) \quad (2.13)$$

where the first term represents the elastic energy contribution and the latter expresses the coupling between the disorder potential *V(r,z)* and the vortex density distribution $\rho(\boldsymbol{r},z)$. Flux lines are considered as point-like objects that possess an equilibrium position R_i (discrete, given the intrinsically periodic nature of the vortex lattice) in the absence of disorder and are displaced in the *xy* plane by a quantity $u_i = u(R_i, z)$. These quantities are two dimensional vectors. Obviously, we expect that the elastic energy depends on the discrete differences between the displacements of two objects, such as u_i-u_{i+1}. An important quantity that characterises the elastic system and can be directly extracted from decoration experiments is the mean squared relative displacement of two vortices separated by a distance r:

$$\mathrm{B(r)} = \overline{<[\mathrm{u}(0,0)-\mathrm{u}(\mathrm{r},0)]^2>} \quad (2.14)$$

---

[1] α,β are the in plane coordinates

where the symbols < > and — denote an average over thermal fluctuations and quenched disorder, respectively. The growth of B(r) with distance measures how fast the lattice is distorted.

Related to B(x) is the structure factor of the lattice that is defined as the Fourier transform of the following quantity:

$$\rho(x) = \Sigma_i\, \delta(r-R_i-u_i(R_i,z)) \qquad (2.15)$$

$\rho(x)$ expresses the density of flux lines.

Diffraction experiments (such as neutrons or x-rays) measure the square of the modulus of the structure factor ($|\rho_K|^2$) and, for a perfect lattice, the diffraction pattern is made of δ functions (Bragg peaks) positioned at the reciprocal vectors of the lattice.

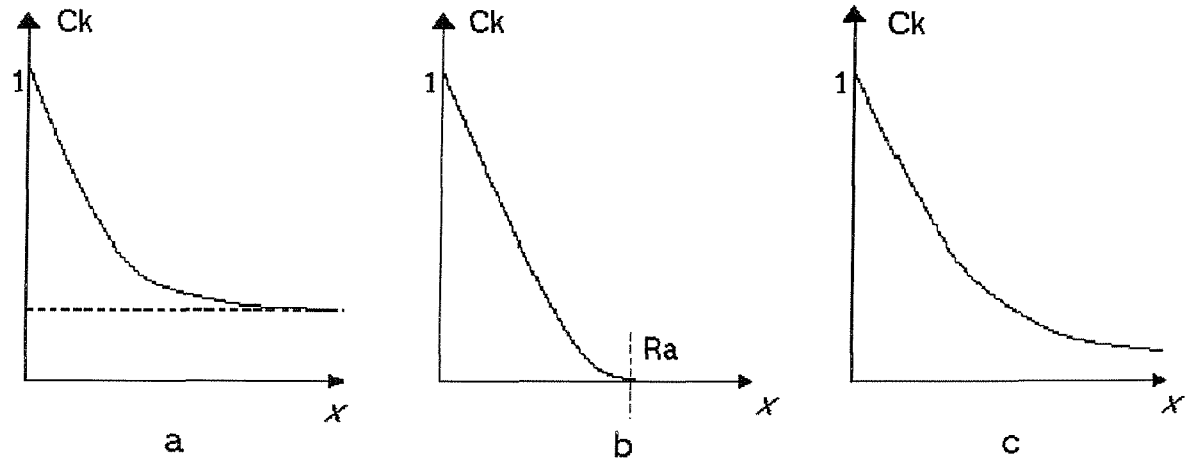

Fig. 2.3. Various possible decays of $C_K(x.)$. a) Case for thermal fluctuations alone. b) The structure factor has no divergent peaks anymore and translational order is destroyed beyond length R_a.. Some degree of order persists at short distance. c) $C_K(x)$ decays as a power law: quasi–long range translational order is retained [from Ref. 38].

Another important quantity is the ***translational order correlation function***:

$$C_K(x) = \overline{< e^{iKu(x)}\, e^{-iKu(x)} >} \qquad (2.16)$$

This is obtained by filtering a single peak centred around the reciprocal lattice vector ***K*** and Fourier transforming it back. In the same way in which in the reciprocal space the shape and the width of any single peak is a measure of the degree of translational order in the lattice, $C_K(x)$ in the lattice space is a direct measure of the residual order in the system. In fact, the broader the peak the faster the decay of $C_K(x)$. Three possible decays of $C_K(x)$ are shown in Fig. 2.3. In particular, the first case represents the situation of a perfect lattice influenced only by thermal fluctuations.

The full solution of the problem is given by a variational method originally developed to study elastic manifold in random media [33], but similar results have been obtained with the renormalization group theory [31] and also with different approaches [34].

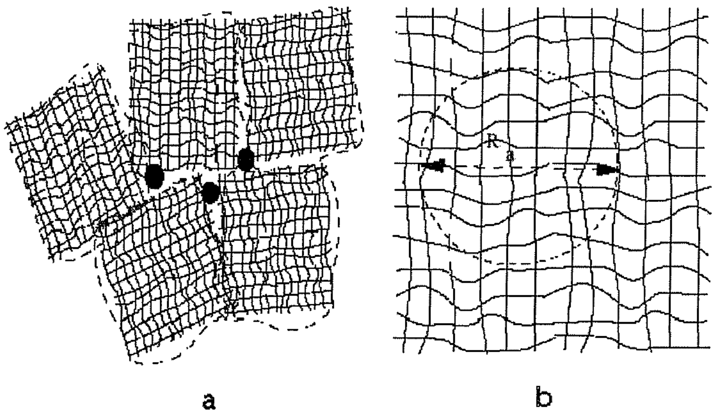

Fig. 2.4. a) Incorrect view of a disordered elastic system. R_a would correspond to a length above which transational order is destroyed and the system would break into crystallites. Black dots represent topological defects b) Bragg glass is the real situation for weak disorder. R_a is the length above which the displacements grow very slowly becoming bigger than a_0. Note that the system preserves quasi-long range translational order and topological defects are not present [from Ref. 38].

The most surprising result is that the periodicity helps the system to maintain quasi long-range translational order. In fact, it is possible to show that $B(r) \approx \log|r|$ and $C_K(r)$ has a slow algebraic decay (case c in Fig. 2.3). Furthermore from an energy argument it can be demonstrated that dislocations are not generated by small enough amounts of disorder. This implies stability of an elastic solution and thus the existence of a thermodynamic glass phase (with many metastable states) retaining a nearly perfect translational order and a full topological order with the six nearest neighbour for every vortex. Since this phase exhibits Bragg peaks as a perfect lattice it is called ***Bragg glass*** (see Fig. 2.4).

Note that the Bragg glass phase is a more particular case than the so-called ***hexatic phase*** often found in literature (see for example Ref. 35) which reflects only the absence of topological order.

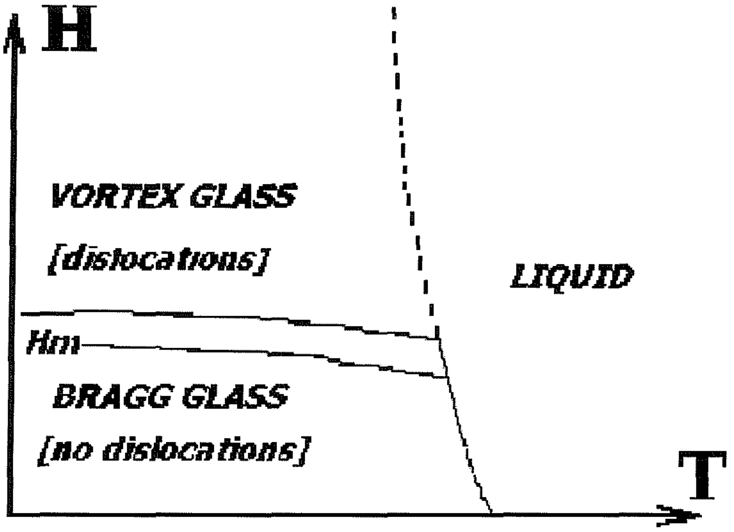

Fig. 2.5. Stability region of the Bragg glass phase in the H-T plane. The thick lines are expected to be first order, whereas the dotted line should be second order. Upon increasing disorder the field induced melting H_m happens for lower fields [from Ref. 38].

It is interesting to note that the existence of Bragg glass has many experimentally observable consequences. In fact, since it has translational order like a perfect lattice it should melt through a first order phase transition. Neutron experiments (that directly measure $C_K(x)$) can be interpreted in term of a Bragg glass and similarly the low field phase seen in type II (HTS and LTS) superconductors. Another interesting consequence, connected to this, is the modification of the H-T phase diagram. The existence of Bragg glass imposes the presence of a transition in field into a different phase containing topological defects when disorder is increased. This is because increasing the field is equivalent to increasing disorder. The high field phase (***Vortex glass***) should melt more continuously into a liquid, and thus it is consistent with the gradual transition observed at high fields. All these considerations lead to a new phase diagram depicted in Fig. 2.5. Its main features should be relevant for all type II superconductors. Note that upon increasing the disorder the field-induced melting occurs for lower fields as indicated in the figure.

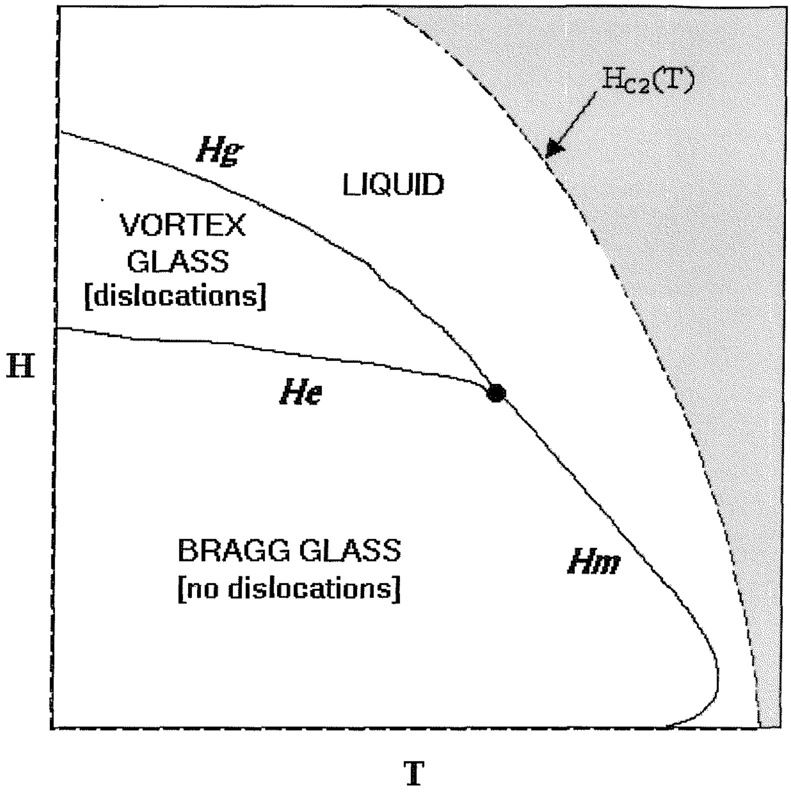

Fig. 2.6. Expected vortex phase diagram for a HTS in the presence of weak random point disorder for B ⊥ layers. In the diagram are indicated the distinct phases. Note the presence of a multicritical point that connects different boundary lines.

The region of stability of Bragg glass will be destroyed when the displacement of nearest neighbour vortices become of the order of the lattice spacing. This fact can be observed due to the combined displacement of both disorder and thermal fluctuations. This means that there are two ways of destroying the Bragg phase. The first is increasing the temperature so that thermal fluctuations give raise to a melting of a solid into a liquid. Alternatively, on increasing the magnetic field disorder induced displacements increase producing a so-called ***solid entanglement*** transition. Such a field driven transition corresponds to the destruction of Bragg glass by the proliferation of topological defects. Thus, the GLeD theory predicts correctly the existence of two distinct transition lines which delimit the region of Bragg glass stability: a vortex solid-to-liquid melting and a vortex solid-to-solid entanglement line.

In Fig. 2.6 a schematic representation of the theoretically predicted vortex phase diagram for an high T_C superconductor is shown. In this diagram all the expected distinct phases are indicated:

1. The lattice melting line, $H_m(T)$ between the Bragg glass and the vortex liquid. Experimental results confirm that this is a first order transition .
2. The glass melting line, $H_g(T)$ between the topologically disordered vortex glass and the vortex liquid. It is expected to be a second order or a continuos transition.
3. The vortex entanglement line, $H_e(T)$ between the Bragg glass and the vortex glass. Magnetisation measurements on BSCCO seem to provide indications for a first order transition [36], as it is supposed to be an order-disorder transition.

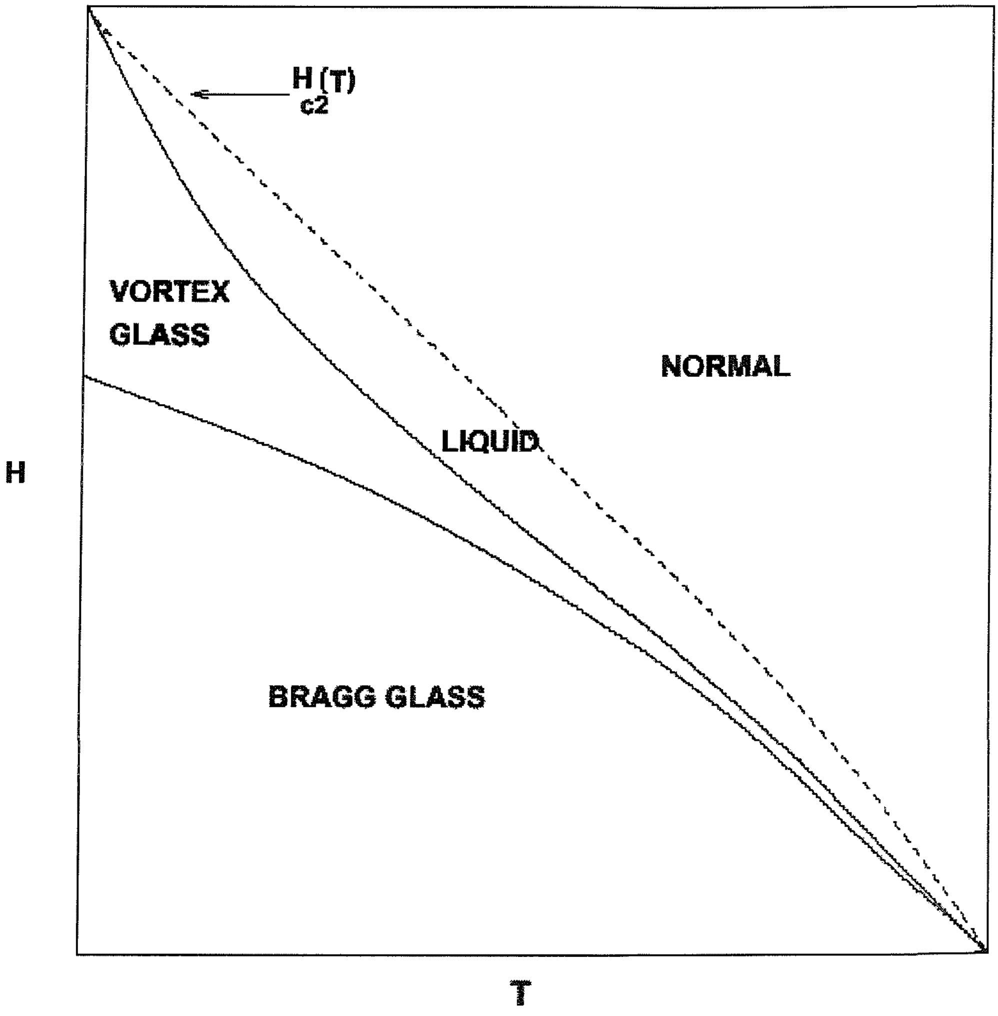

Fig. 2.7. Phase diagram for a low T_c type II superconductor incorporating the effects of thermal fluctuations and quenched disorder.

These lines can be predicted using a generalised Lindemann criterion in which the pinning energy induced by point defects is included. All the lines are obtained by balancing the appropriate characteristic energies: $E_{v\text{-}v}$ (vortex-vortex interaction or elastic energy), E_p (pinning energy) and E_{TH} (thermal energy). For example this treatment was carried out by Nelson and Vinokur [37]. Their model is used in chapter 4 to interpret the experimental data obtained in this thesis on YBCO.

It is worthwhile noting in the diagram the presence of a multicritical point, i.e. a point of convergence of different boundary phase lines. In the case in which the role of pinning is enhanced with respect to thermal fluctuations the critical point can be shifted up until the critical temperature T_c. Therefore the first order melting line of the solid can disappear and thus the quasi ordered solid transforms in a true glass at all temperatures.

Note also that this diagram can only be attributed to an HTS. For a conventional low T_C superconductor with random point pinning disorder we expect a phase diagram as that shown in Fig. 2.7 [39]: in this case the Bragg glass melting transition is separated from the thermal melting line and thus a true glass phase is present for all $T<Tc$. This difference should be connected with the enhanced importance of thermal fluctuations in HTS that can push down the thermal transition to lower temperatures merging in part the Bragg glass melting line. Chapters 4 and 5 show how much these phase diagrams correspond to our experimental findings on the HTS YBCO and the LTS $NbSe_2$.

References

1 A. M. Campbell and J. E. Evetts, Adv. Phys. **21**, 129 (1972).

2 L.F. Cohen and H. J. Jensen, Rep. Prog. Phys. B **60**, 1581 (1997).

3 E. H. Brandt, Rep. Prog. Phys. **58**, 1465 (1995).

4 M. Thinkam, Introduction to Superconductivity Second Edition (Mc Graw-Hill, 1996).

5 J. Bardeen and H. J. Stephen, Phys. Rev B **140**, 1197 (1965).

6 C. F. Hempstead and Y. B. Kim, Phys. Rev. Lett. **12**, 145 (1964); Y. B. Kim et al., Phys. Rev. B **139**, A1163 (1965).

7 A. I. Larkin and Yu V. Ovchinnikov, J. Low Temp. Phys. **34**, 409 (1979).

8 A. Pippard, Phil. Mag. **19**, 217 (1969).

9 M. Tinkham, Helv. Phys. Acta **61**, 443 (1988).

10 R. M. Langan et al., Phys. Rev. B **58**, 14548 (1998).

11 S. Fleschler, Phys. Rev. B **47**, 14448 (1993).

12 C. J. van der Beek et al., Phys. Rev. B **51**, 15492 (1995).

13 Ravikumar G. and al., Physica C **276**, 9 (1997).

14 K. Gosh et al., Phys. Rev. Lett. **76**, 4600 (1996).

15 P. W. Anderson, Phys. Rev. Lett. **9**, 309 (1962).

16 P. W. Anderson and Y. B. Kim, Rev. Mod. Phys. **36**, 39 (1964).

17 Y. Yeshurun and A. P. Malozemoff, Phys. Rev. Lett. **60**, 2202 (1988).

18 G. Blatter et al., Rev. Mod. Phys. **66**, 1125 (1994).

19 $\varepsilon=1/\gamma$. m and M denote as in chapter 1 the (small and large) effective electronic masses in the ab plane and along the c axis, respectively.

20 G. Eilenberger, Phys. Rev. **164**, 928 (1967).

21 A. P. Malozemoff and al., Phys. Rev. B **38**, 7203 (1988).

22 H. Safar and al., Phys. Rev. Lett. **70**, 3800 (1993).

23 E. Zeldov and al., Nature **375**, 373 (1995).

24 A. Schilling et al., Nature **382**, 791 (1996).

25 M. P. A. Fisher, Phys. Rev. Lett. **62**, 1415 (1989).

26 J. A. Mydosh, Spin Glasses: An Experimental Introduction (Taylor and Francis, London, 1993).

27 D. S. Fisher et al., Phys. Rev. B **43**, 130 (1991).

28 M. Feigelman et al., Phys. Rev. Lett. **63**, 2303 (1989).

29 D. G. Grier al, Phys. Rev. Letter **66**, 2270 (1991).

30 T. Giamarchi and P. Le Doussal, Phys. Rev. Lett. **72**, 1530 (1994).

31 T. Giamarchi and P. Le Doussal, Phys. Rev. B **52**, 1242 (1995).

32 T. Giamarchi and P. Le Doussal, Phys. Rev. B **55**, 6577 (1997).

33 M. Mezard and G. Parisi, J. Phys. I (France) **4**, 809 (1991).

34 D. S. Fisher, Phys. Rev. Lett. **78**, 1964 (1997).

35 D. Grier et al., Phys. Rev. Lett. **66**, 2270 (1991).

36 B. Khaykovic et al., Phys. Rev. Lett. **76**, 2555 (1996).

37 D. R. Nelson and V. Vinokur, Phys. Rev. B **48**, 13060 (1993); A. I. Larkin and V. Vinokur, Phys. Rev. Lett. **75**, 4666 (1995).

38 T. Giamarchi and P. Le Doussal, cond-matter/9705096.

39 S. S. Banerjee et al., cond-mat/0007451.

Chapter 3

Experimental Techniques

The results presented in this work were obtained using DC transport and magnetic techniques. In this chapter we will briefly review the main characteristics and differences between these two ways of investigating the vortex-state of a type II superconductor. In particular, large attention is paid to two arrangements used in the context of magnetic measurements: the vibrating sample magnetometer (VSM) and the torque magnetometer. Finally, in sections 3.3 and 3.4 a description of the two specific experimental set-ups used is provided: the Helium-3 insert and the Grenoble High Field Transport Arrangement. Particular emphasis has been given to the first arrangement as it was for the first time introduced at the University of Southampton with personal involvement by the author of this thesis.

In general, a wide variety of different experimental approaches can be used to probe static and dynamic properties of vortices in type II superconductors. The most important are:

1. Direct current transport measurements
2. Magnetisation measurements: Vibrating sample magnetometry, ac susceptibility, mechanical oscillator and torque magnetometry, all belong to this category.
3. Calorimetric measurements (like DSC and DTA)
4. Structural studies including neutron beam diffraction, scanning tunnelling microscopy and Hall probe microscopy

Each of these techniques has its own particular range of usefulness. We will not discuss all these different methods in detail here but will focus our attention on transport and some magnetic techniques.

3.1 Transport Measurements

When a simple measurement of the resistance of a sample is performed by attaching two wires to it, one inadvertently also measures the resistance of the leads and of contact point of the wires to the sample. Typically these last contributions are smaller than the resistance of the sample. However, when one is measuring a very small sample resistance these contact contributions can dominate and completely obscure changes in the resistance of the sample itself. This is the situation that exists when working with

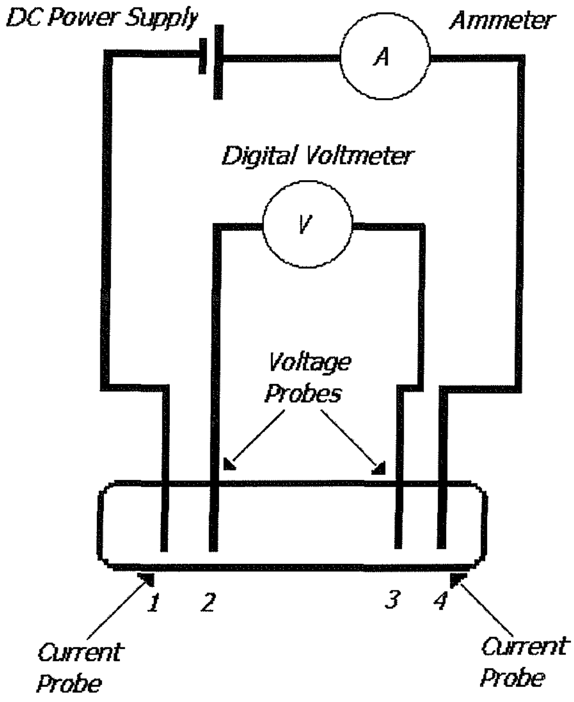

Fig. 3.1. Schematic illustration of a four point configuration.

superconductors. The effects of the contact and lead resistance can be eliminated with the use of a four terminal transport technique. In this case a sufficiently large current flow is passed on the sample by attaching current leads (this can be easily done using a current source or a power supply). We have seen that the flow of current produces a motion of the vortex-lines generating a dissipative voltage. This voltage drop is directly measured via the other two contacts. Fig. 3.1 shows a schematic of a four-point configuration. Using this method, only the resistance (ratio of the voltage registered on a digital voltmeter to the value of the driving current) contribution originating from the sample itself is measured.

With transport measurements it is possible to investigate the part of the H-T phase diagram near the transitions Normal-Superconductor and vortex-liquid to vortex-solid. Well below (in T and H) these transitions, the vortex system becomes strongly pinned and the maximum transport current that can be applied is insufficient to move flux lines and thus to produce a measurable voltage. In contrast, in this strongly pinned region, magnetisation measurements are most useful.

The most important limitations of the transport technique are related to the practical constraints of attaching contacts, passing large currents through these contacts and measuring small voltages (10^{-8} V). Working with a very low resistance measurement circuit is very important as it is the best way of limiting intrinsic (Johnson) noise. This means reducing lead resistance (typically around 10 ohm) and sample contact resistance (that should be of the order of 1 ohm). In practice, it is very difficult to reduce the lead resistance below a certain level because the use of wires with bigger cross sectional area in a cryogenic system has the disadvantage of unacceptably enhancing the heat transfer and the boil-off rate. For this reason it is of vital importance to reduce the resistance of the sample contacts. Furthermore, insufficiently low resistance can give raise to local heating (Joule effect) effects and hence unwanted temperature gradients across the sample.

Finally, it is worth noting that a transport measurement cannot be rigorous proof of a phase transition that, being a thermodynamic phenomenon, can be checked by observing a discontinuous change in some thermodynamic variables.

3.2 Magnetic Measurements

Generally speaking, in a magnetisation experiment an applied magnetic field is swept, inducing a current density ***J*** in the material. This current produces a magnetic moment that can be easily measured. The relation between the magnetic moment and the current density is not trivial and attention is needed to take into account sample geometry effects. Certainly, the most important advantage of a magnetic measurement is the fact that this method is contactless.

3.2.1 Torque Magnetometer

The most commonly used method of measuring magnetocrystalline anisotropy is torque magnetometry. In anisotropic and low dimensional magnetic materials, the magnetisation is a vector quantity and depends upon the direction as well as the magnitude of the applied magnetic field. Torque magnetometry exploits the anisotropy of high T_c superconductors. In fact, the application of a magnetic field $\boldsymbol{B}$ not parallel to the c axis on a high T_c specimen produces a magnetic moment with a normal component perpendicular to the magnetic field itself. Hence, a finite torque is exerted on the sample:

$$\frac{\tau}{V} = \boldsymbol{M} \times \boldsymbol{B_a} \qquad (3.1)$$

where V is the volume of the sample, $\boldsymbol{M}$ the magnetisation and $\boldsymbol{B_a}$ the applied magnetic field. The sample is fixed on a mobile arm of a metallic capacitor and when it feels the exertion of a finite torque it deforms the capacitor elastically. If the deflection angles are small, a linear relation between the change δC and the torque τ exists and it is possible to obtain the projection of the magnetisation vector on the c axis.

We can represent this change due to the torque as the presence of an extra capacitance $C(\tau)$ connected in series. Therefore the initial C_i of the system is changed in:

$$\frac{1}{C_{total}(\tau)} = \frac{1}{C_i} + \frac{1}{C(\tau)} \qquad (3.2)$$

Supposing that $C(\tau) >> C_i$, $\delta C(\tau)=C_{total}(\tau) - C_0$ becomes

$$\delta C(\tau) = -\frac{C_i^2}{C(\tau)}. \tag{3.3}$$

For the configuration showed in Fig. 3.2 and for small angular deflection θ, C(τ) is given by [1]

$$C(\tau) = C(\theta(\tau)) = \frac{\varepsilon_0 l}{\theta} \ln\frac{R}{r} \tag{3.4}$$

where ε_0 is the permittivity of vacuum and l, R and r are defined in the Fig. 3.2. Substituting eq. (3.4) in eq. (3.3) we obtain

$$\delta C(\tau) = -\theta \frac{C_i^2}{\varepsilon_0 \ell \ln(R/r)} \tag{3.5}$$

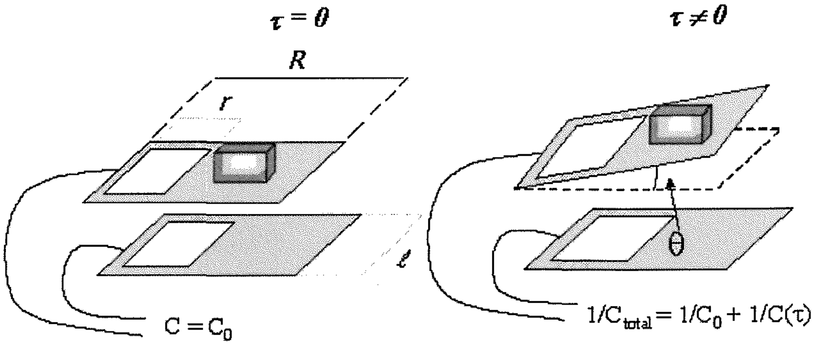

Fig. 3.2. Schematic drawing of a two-arm capacitor system without and with a small deflection of its mobile arm.

Since θ is proportional to the torque, it is evident from this result that measuring δC(τ) means measuring τ (they are linearly related) and thus the magnetisation of the sample. Obviously, in order to obtain absolute values of the torque it is necessary to calibrate the magnetometer with a sample of known dimensions and magnetic moment. A torque magnetometer was mounted inside the Grenoble High Field Transport Arrangement described in section 3.3.

3.2.2 Vibrating Sample Magnetometer

The Vibrating sample magnetometer is a piece of standard equipment used for the magnetic characterisation of thin films, structures and superconductors. In Fig. 3.3 a schematic illustration of the measuring apparatus of a VSM is shown. The system is designed to detect an ac field produced by the magnetic moment of a sample that is vibrated in a controlled manner (frequency f = 66.6Hz), in a constant magnetic field. The detecting tool consists of a pair of pick-up coils that are opposite connected in series. This particular configuration eliminates problems arising from magnetic field instability or mechanical vibrations of the magnet.

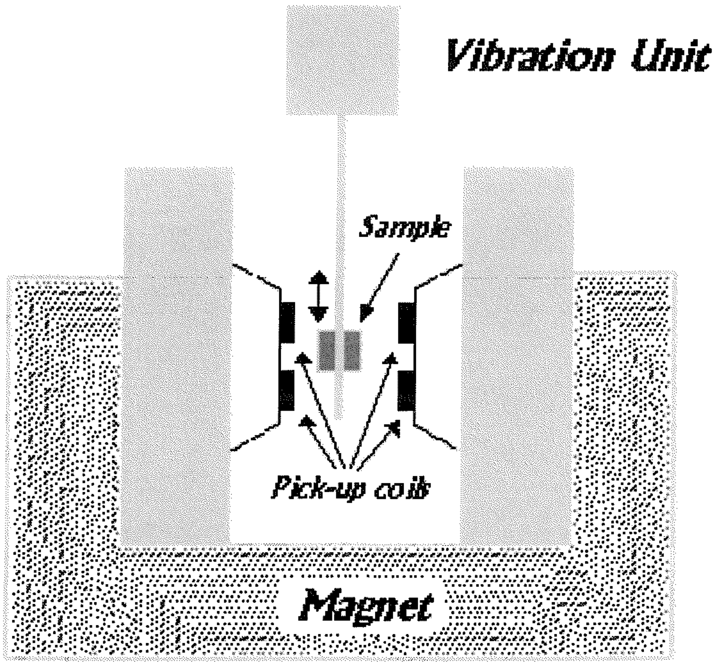

Fig. 3.3. Schematic illustration of a Vibrating Sample Magnetometer.

Lentz law applied to this system states:

$$\varepsilon = -d\Phi(t)/dt \qquad (3.6)$$

where $\Phi(t)$ is the varying magnetic flux produced by the magnetic moment of the sample and ε is the induction voltage across the terminals of the two detecting coils. If the specimen is homogeneously magnetised and small enough to be considered as a dipole, it can be easily demonstrated that [2,3]:

$$\varepsilon = -\frac{d}{dt}\left[\int \frac{\mathbf{M}\cdot\mathbf{B}}{I}dV\right] \tag{3.7}$$

Assuming the position of the sample along the vibration axis as $z(t) = z_0 + z_a\cos(\omega t)$ (z_0 and z_a being the mean point and amplitude of sample oscillation respectively) the induced emf becomes:

$$\varepsilon = z_a\omega\sin(\omega t)\int M_z\frac{\partial}{\partial z}\left(\frac{B_z}{I}\right)dV = z_a\omega\sin(\omega t)\int M_z G(z)dV \tag{3.8}$$

where $G(z) = \frac{\partial}{\partial z}\left(\frac{B_z}{I}\right)$ is the so called *sensitivity function* that represents the dependence of the VSM output on the position of the sample along the z-axis. Using the dipole approximation it is possible to expand G(z) into a power of series about the equilibrium position z_0 in order to obtain:

$$\varepsilon \approx z_a\omega m G(z_0)\sin(\omega t) \tag{3.9}$$

where m is the magnetic moment of the sample and $G(z_0)$ is the zero order term. This formula demonstrates that an increase in sensitivity of the measurement is reached designing the coils-configuration to obtain the highest G(z) values as possible. A typical form of this function is shown in Fig. 3.4 where the point $z_0=0$ is taken in the middle of the coils.

Note that from (3.9) it is possible to calculate the magnetic moment of the sample only if the value of $G(z_0)$ is known. For this reason the instrument has to be calibrated with a specimen of known magnetic properties. One of the most common materials for this purpose is Nickel because it has a small saturation field and it can be obtained in high purity.

For this work, at the University of Southampton, we used a commercial Oxford Instrument Aerosonics 3001 [4]. It allowed us to measure the magnetic moment of a sample as a function of time, field and temperature, for fields up to 12 Tesla in a range from 2.1K to 300K. An important component of this system is the cryostat that is kept cold by a vacuum isolation (10^{-4} Torr) and two vessels: the first filled with liquid helium and the second with liquid nitrogen. The aim of this liquid nitrogen jacket is to shield the helium (that possess a very low latent heat of vaporisation) from the thermal radiation emitted by the external environment. The outer surface of both vessels is covered by a multilayer superinsulation which drastically reduces thermal conductivity. The constant magnetic field is produced by two concentric solenoids of Niobium Titanium (NbTi) and Niobium Tin (Nb_3Sn) placed in the helium vessel. The produced field has a homogeneity of 0.1% over a 10mm diameter sphere. Finally the operation of the VSM is fully automated by the use of commercial software written by Aereosonic. This software runs on a PC and operates via a RS 232 serial interface.

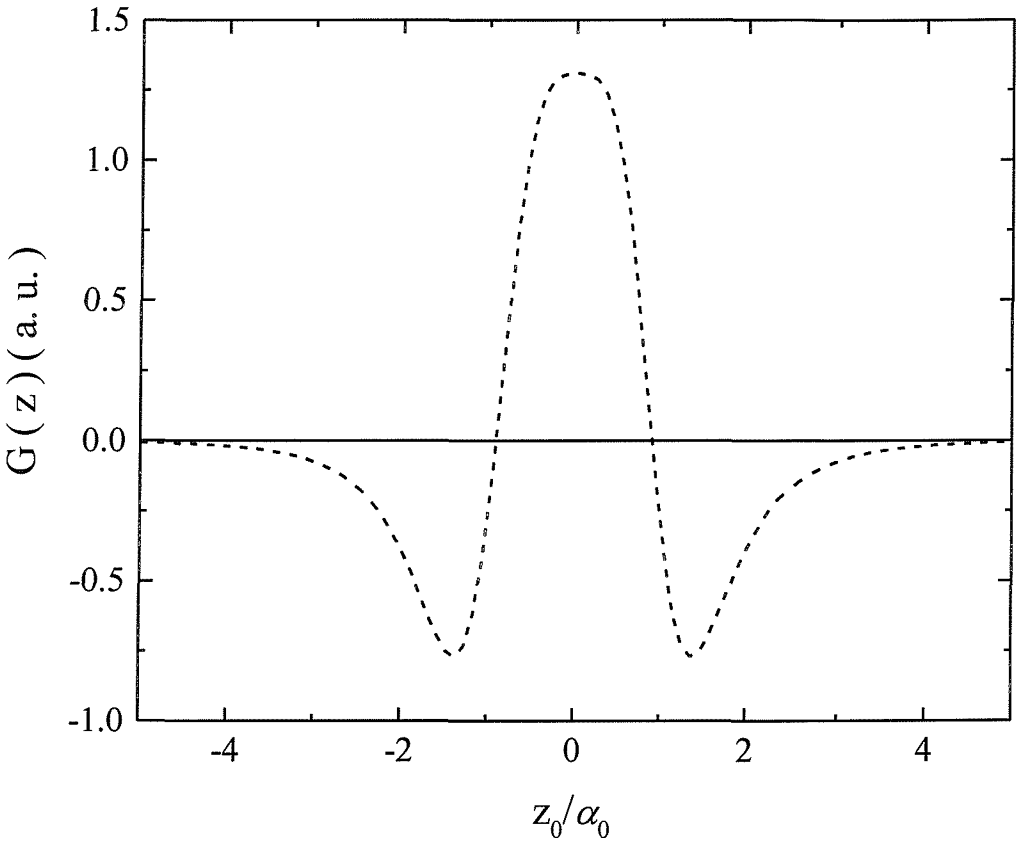

Fig. 3.4. Sensitivity function G(z) calculated for the case of a dipole parallel to the z axis and a coil geometry like in Fig 3.3. G(z) has a maximum at $z_0=0$.

3.3 Oxford Instrument ^{3}He Insert

The Oxford Instrument ^{3}He Insert is a cryogenic system designed to reach a minimum temperature of 0.27 K. In order to operate, it must be mounted in a bath of liquid ^{4}He in a pre-existing cryostat. No description is given here of this vacuum insulated liquid helium ("standard") cryostat whose main operating characteristics are the same as the VSM briefly discussed in the previous paragraph.

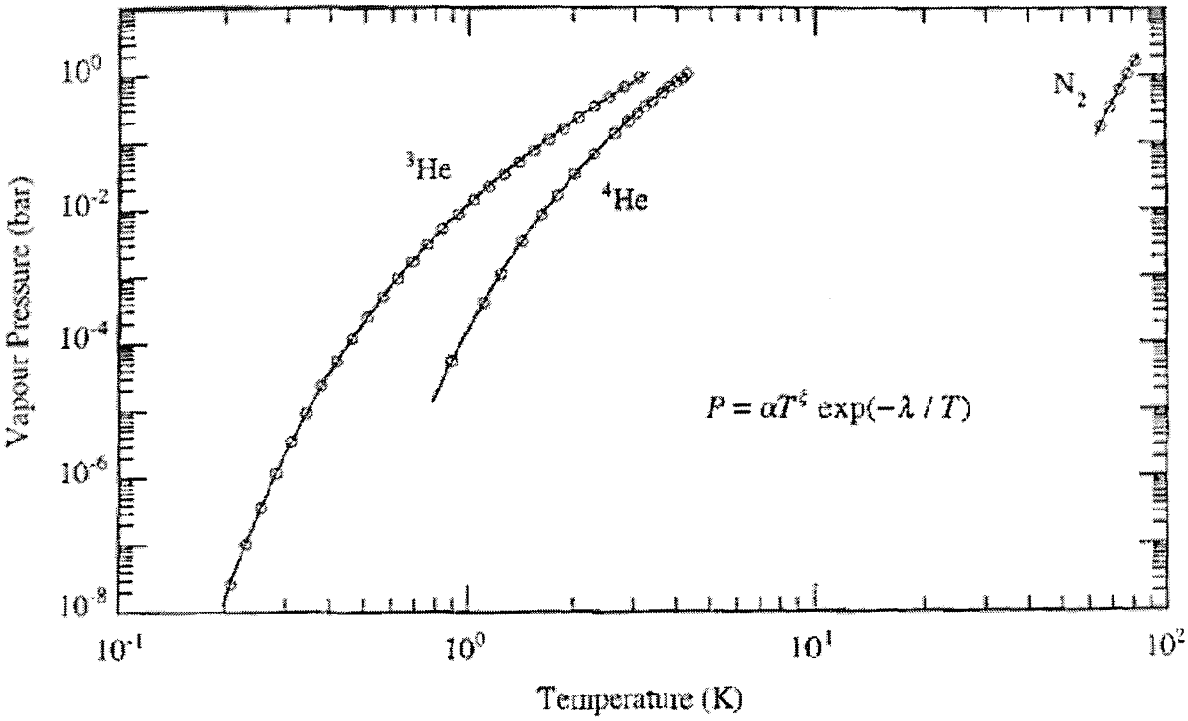

Fig. 3.5. Measured (points) and approximated (curves) behaviour of the saturated vapour pressures of the most common cryogenic liquids. The curves are plotted with the equation shown that has different parameters α, λ, ξ for each liquid.. The approximations are reliable only in the range defined by the plotted curves.

In Fig. 3.5 the behaviour of saturated vapour pressure for some common cryogenic fluids is illustrated [5]. The difference between the two P-T curves of helium explains the reason for which by reducing the pressure of ^{3}He it is possible to reach temperatures lower than 1K. Note that ^{3}He is a much more expensive isotope than ^{4}He and thus it is extremely crucial to rely on a system that reduces leaks to a negligible level, allowing complete recovery of the gas.

In Fig. 3.6 a schematic view of the main parts of the ^{3}He system is shown, illustrating the two stages used in this rig. The sorption pump (sorb) is cooled drawing liquid helium from the main bath through a heat exchanger pumping line. It absorbs ^{3}He gas when cooled below 40K and the amount of gas that can be absorbed depends upon its temperature. It reaches its best performances around 8K.

The 1K pot is mounted below the sorb and it has two main purposes:

- condensing the ^{3}He gas during the condensation phase
- reducing the heat conducted to the sample space to a minimum when the ^{3}He vapour pressure has been reduced to cool the sample.

The 1K pot is fed from the main bath by a needle valve. Sorb and pot are completely surrounded by a vacuum chamber (IVC) that provides isolation from the liquid helium bath. The temperatures of both are measured by two carbon glass thermometers and stabilised by energising separate heaters. The heater outputs to the temperature control loops were controlled using two different Oxford Instruments ITC-4 temperature controllers.

The ^{3}He is stored in a dump vessel contained in a separate box (gas handling system) equipped with a pressure gauge that monitors the amount of gas. Before starting the experiment, the dump has to be directly connected to the cryostat and, in particular, to the sample space using a metallic tube and a Hoke valve. The sample space runs through the centre of the system (Fig. 3.6) and it is necessary to keep it isolated from the external environment. For this reason, a vacuum lock is provided to allow the sample to be inserted and withdrawn, without loosing any ^{3}He or allowing any air to enter.

The probe is equipped with two coaxial cables and twenty constantan wires that are connected to the top electrical access of the cryostat. The sample is mounted on a small cylindrical block at the end of the top loading probe which is designed to load it directly into the liquid ^{3}He (that condenses at the bottom of the sample space as in Fig. 3.6) through the central access of the system. The sample block is made of brass and has a diameter of about 20 mm. This space is hardly enough for positioning the sample, a heater and a Speer thermometer. In addition, two copper screws were bolted to this block to provide a better thermal connection between the sample and the reservoir of liquid ^{3}He. The heater outputs were controlled by means of a Lakeshore 340 temperature controller that has the facility to fully optimise the temperature control, storing multiple sets of PID feedback parameters for different ranges of temperatures.

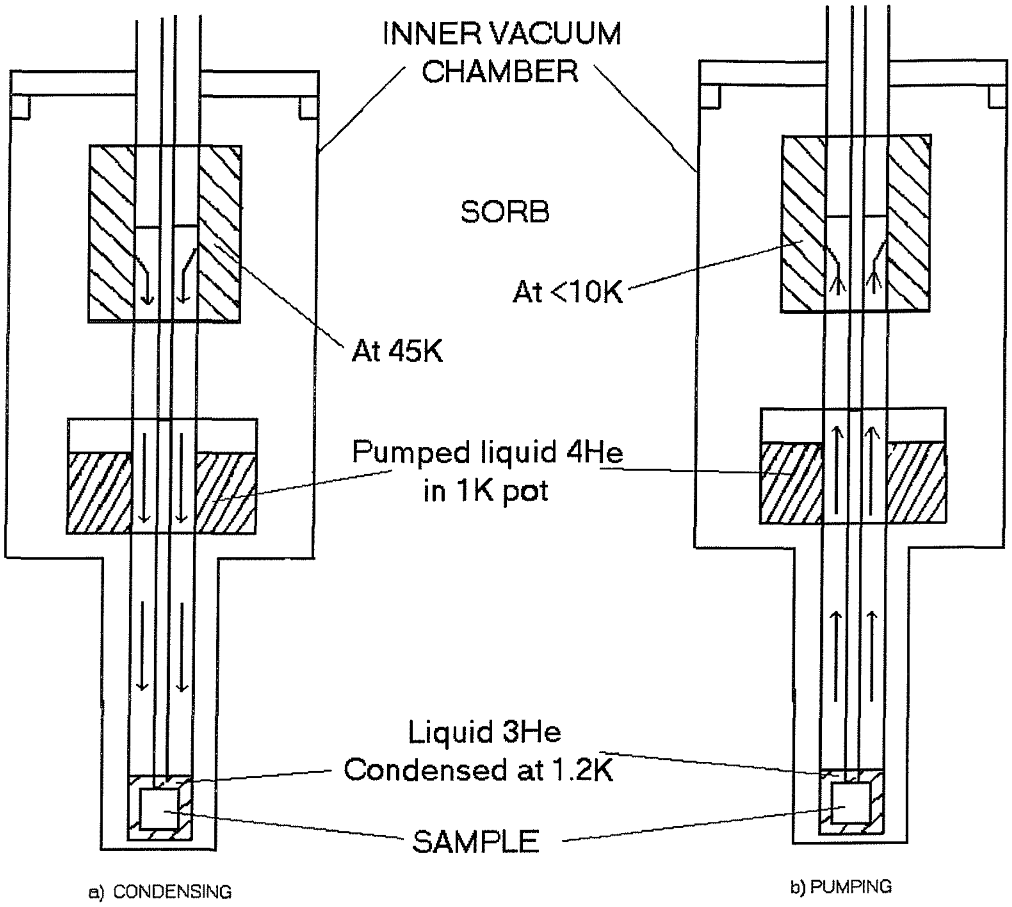

Fig. 3.6. Operating principle of a sorption pumped ^{3}He refrigerator

The procedure of operating the system is the following. Before inserting the sample, the sorb is warmed to above 40K so that it will not absorb gas and will release absorbed gas. After the insertion of the probe, the ^{3}He is allowed in the sample space (Fig. 3.6-a). It condenses on the 1K pot and runs down to cool the sample. When all the gas enters the sample space the 1K pot is left to cool to the lowest possible temperature. Then, all the gas condenses and the pressure drops to a few mbar. At this stage the sample is in close contact with liquid ^{3}He at 1.2K. To obtain lower temperatures now the sorb has to be cooled, thus reducing the vapour pressure above the liquid ^{3}He (Fig. 3.6-b) and lowering the sample temperature. With this procedure a minimum temperature of 0.27K is reached.

When it becomes impossible to reach the lowest temperature it is very likely that the ^{3}He gas is running out. In this case, it is necessary to heat the sorb at a temperature higher than 40K. By doing this, the sorb will release the gas allowing it to condense again at the bottom of the sample space. As soon as all the gas has been desorbed, the vapour pressure can be reduced in order to lower the temperature of the sample.

The ^{3}He can be left in the insert and collected after some days at the end of the experiment. In order to recover all the gas it is necessary to apply heat to the sorb and to the reservoir at the bottom of the sample space, boiling-off any remaining liquid ^{3}He. To remove all the remaining gas a cryopump (a long metallic cylinder that can store up to two litres of gas) is used. It is directly connected to the gas handling box. Lowering this tool into a dewar of liquid helium at 4.2K allows all gas left in the insert to be collected.

A schematic layout of the full experimental arrangement used in conjunction with the ^{3}He apparatus is shown in Fig. 3.7. The magnetic field is supplied by an high field superconducting magnet (Oxford Instrument cryomagnet) that can provide fields up to 14 T (T= 4.2K) and 16T (T= 2.2K). Excluding the sorb and the pot that have been controlled (manually) with the use of two different ITC-4 temperature controller, the rest of the experiment is directly run by means of purpose written control software programs developed by the author of this thesis. These programs were written using "HP VEE" a graphical programming environment commercialised by Hewlett Packard. Developing different computer programs allowed the execution of many different tasks over the entire experiment. In fact, each program can execute a complex series of experimental steps and record data in ASCII format on the hard disk of the computer. As shown in Fig. 3.7, the instruments communicate with the computer using RS 232 or IEEE interfaces. It is worthwhile noting that, thanks to the versatility of this software and to the re-usability of various parts of the programs, it was possible to easily develop new control programs, designed for other low-temperature experiments, simply by re-utilising (with little or no modifications) various subroutines already written for the ^{3}He experiment.

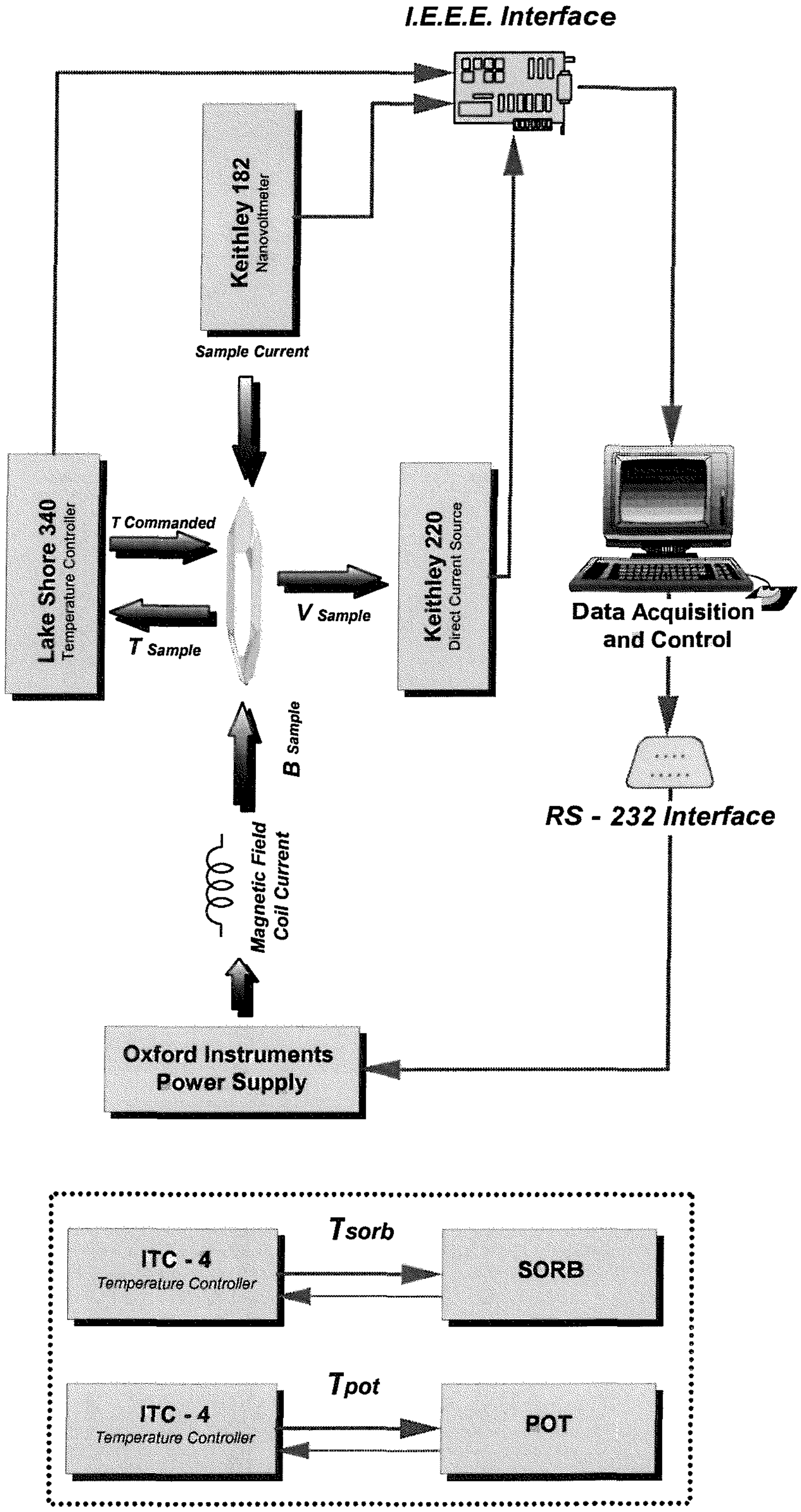

Fig. 3.7. Schematic representation of the experimental set-up used in conjunction with the ^{3}He system for transport studies of 2H-NbSe$_2$.

3.4 Grenoble High-Field Transport Arrangement

The torque data shown in this thesis were acquired at the Grenoble High Magnetic Field Facility [6]. At this research centre various magnetic installations are available providing fields of up 30T [7]. It is possible to reach such high magnetic fields using resistive magnets made with copper based windings of the Bitter type. The Bitter coil is a special configuration designed for reaching very high fields and is illustrated in Fig. 3.8.

Basically, a Bitter coil consists of a stack of circular copper plates all connected but insulated from each other except along a radial slit in the insulation. The current passes from plate to plate producing a constant magnetic field inside the central part of this spiral construction. The cooling of the magnet, necessary to dissipate the heat produced in the arrangement by the Joule effect, is provided by a circulation of de-ionised and de-oxygenated water. As shown in the picture, the holes through which the cooling water is passed are concentrated in the central part of the plates where the current density is the highest. Each magnet is supplied with a voltage of about 400V at full power. The current is provided by power rectifiers which reach a stability of 10 ppm over a period of time of about ten minutes. A control console equipped with a computer is used to control each magnet sending user's instructions to the power sources and checking the quality of the magnet operation several times per second. In this way the user can program the rate of variation of the current (and therefore of the magnetic field) and the field itself.

Finally, the sample temperature is controlled by means of an Oxford Instrument ITC-4 with a single temperature control loop. The thermometer is a Cernox sensor well known for its good reproducibility and in particular its low magnetoresistance.

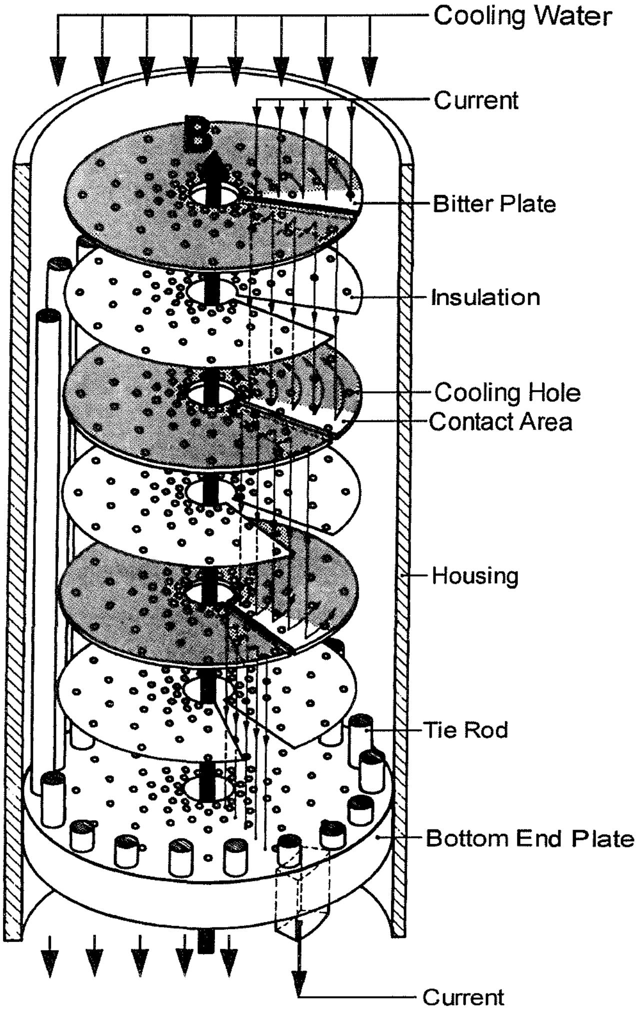

Fig. 3.8. Bitter magnetic assembly used at the Grenoble High Magnetic Field Laboratory [from Ref. 7].

References

1 V. Vulcanescu, Ph. D. thesis (Université Paris-Sud, 1997).

2 J. Mallinson, J. Appl. Phys. **37**, 2514 (1966).

3 H. Zijlstra, Experimental Methods in Magnetism, (North-Holland Publishing Company, Amsterdam, 1967).

4 Vibrating Sample Magnetometer with Superconducting Magnet, System Manual, Oxford Instruments Limited.

5 Notes from Low Temperature Techniques Course (1999). Birmingham.

6 Access obtained under the Training and Mobility of Researchers Programme of the European Community.

7 Grenoble High Magnetic Field Laboratory, *Access to the High Magnetic Field Installation* (1999).

Chapter 4

Phase Diagram near the Multicritical Points in $YBa_2Cu_3O_7$ Single Crystals

4.1 Introduction

It is well known that with increase of the magnetic field (or the temperature) normally the critical current J_C decreases. However, in most classes of type II superconductors it is possible to observe the so called "peak effect" (PE) [1]: an anomalous enhancement of the critical current density J_C. In transport studies this phenomenon manifests itself as a dip in the resistivity versus temperature (or field) curves, whereas in magnetisation measurements it corresponds to a peak in the magnetic hysteresis far above the self-field dominated region. It appears in close proximity of $H_{C2}(T)$ in low-T_C materials and near the flux-line melting line in high-T_C systems and, as we pointed out in chapter 2, it is related to a structural reorganisation of the flux lines, which increases the volume pinning force via a softening of the vortex lattice [2-3]. Recently this peak was found to become narrow in HTS pure crystals and its clear connection with vortex-phase transformations has been demonstrated [4]. Furthermore, recent neutron diffraction studies in Nb [5] have directly shown the existence of a sequence of different vortex-phases through the peak-effect: at the onset of the peak, the quasi-ordered Bragg-glass is destroyed by the proliferation of dislocations and followed by an intermediate phase characterised by the contemporary presence (mixture) of ordered and disordered regions. Above the peak a completely amorphous phase (vortex-glass) is formed. Thus, the PE clearly defines the position of an order-disorder transition, which is believed to be a first order transformation [6].

In this chapter we show magnetisation measurements performed on $YBa_2Cu_3O_7$ single crystals using a sensitive magnetic torque rig and a vibrating sample magnetometer. Studying the behaviour of the PE to determine the position of the above described transition, we obtained the phase diagram of this material. In particular our aim was to clarify the existence of multicritical points on the vortex-melting line $B_M(T)$ where the significance of the term multicritical point describes a point in the B-T plane where several phase boundary lines converge.

We confirm the existence of two such points near which we observe a transition from the first order melting jump in the reversible magnetisation to a very narrow peak (second order transformation) with a width even smaller than the one seen in conventional superconductors. We have demonstrated the existence of history effects below the two multicritical points providing a full demarcation of the Bragg glass phase. Furthermore we found a pronounced symmetry observed in the behaviour of the phase lines, irreversible magnetisation and jump values.

In brief, the structure of this chapter is organised as follows. In section 4.2 experimental details specific to the studies presented in this chapter are described. In section 4.3 we show our magnetisation results. In particular we describe the evolution of the magnetisation curves and of the peak-effect at different temperature ranges extracting the melting line and the multicritical points. This procedure allowed us to map the phase diagram that is presented and discussed in section 4.4. Finally, in section 4.5 we present a summary of our main findings and conclusions.

4.2 Specific Experimental Details

The M versus B curves, presented in this chapter, were performed on the "Grenoble High Field Transport Arrangement" described in chapter 3. Using this system we were able to investigate magnetisation curves up to 28T. In this installation magnetic hysteresis measurements were performed using a cantilever capacitive torque meter. This device is much more sensitive than conventional magnetometers especially at high magnetic fields. In order to obtain the magnetic moment from the collected values of the torque τ, we used the known relation $m = \tau/B\sin\theta$, where θ is the small angle (1-15 degrees) between the applied magnetic field and the c-crystalline axis. Due to the geometrical confinement of the shielding currents in thin samples (like ours) the direction of the moment essentially is the direction of the c-axis [7]. The signal from the capacitive plates was acquired via a Stanford SR530/830 lock-in amplifier.

The procedure of calibrating the torque capacitance is as follows: after measuring the signal from the sample at fixed angle θ_F and temperature T_F, this curve is compared with the curve obtained with a VSM at the same temperature T_F on the same sample. There is always a good correspondence between the graph from the VSM and the graph from the torque. From the corresponding absolute values of the magnetisation given by the VSM the torque data can be recalculated. The sweep rate of our measurements was 60 mT/s. We controlled the temperature with a specialised capacitive bridge set-up (Lakeshore). Temperature stabilisation was achieved using a capacitive thermometer. For reasons of its low magneto-resistance and high sensitivity over the temperature range studied, Cernox sensor was used for our measurements of sample temperature.

In order to demarcate the Bragg glass phase and collect history dependencies, magnetisation measurements were performed using our *Oxford Instruments* vibrating sample magnetometer for applied fields up to 12 T with a sweep rate of 5 mT/sec. Studies of the single crystals were carried out for the usual configuration of fields applied along the c-axis.

We have studied three flux-grown $YBa_2Cu_3O_y$ single crystals [8]. They were prepared in three different groups using Y stabilised Zr and Y_2O_3 crucibles, a process that gives crystals of excellent purity [9]. Crystal ZY was in an as-grown untwinned state. Two others, named AS and D3, were detwinned by applying a uniaxial pressure These crystal were analysed by polarised light microscopy and they did not show any twin planes. Using high (370-460bar) oxygen pressure annealing at low (400-500°C) temperature for a long period (120-160hrs) all the crystals were oxidised to the state y=7 with deficiency less then 0.003 according to the isotherms [10]. Data is presented mainly for ZY sample which has the largest dimensions and was also used for detailed history dependence studies with the VSM. In any case the displayed results are typical for all the studied crystals.

4.3 Peak Effect and Determination of the Characteristic Points.

Depending on the sample and on the oxygen content, the vortex-melting transition has been reported to be of first or second order. By the Ehrenfest's classification with a first order phase transition we mean a discontinuity in the first derivatives of the free energy F: a jump in the entropy ΔS and a jump in the magnetisation ΔM by varying either of the control variables T or H. Instead, second order means a discontinuity in the second derivatives of F, i.e. a jump ΔC in the specific heat accompanied by a break in the slope of the magnetisation. It is well known that the vanishing irreversibility above the peak in the magnetisation corresponds to a second order transition from a disordered vortex-solid to a vortex-liquid. Furthermore it has recently been demonstrated that, like the onset of the peak effect, history effects in the magnetisation loops mark a destruction of the quasi-ordered Bragg-glass phase [11].

The peak effect in high temperature superconductors has been a subject of intensive study since its discovery in 1991 [12] but numerous research on the peak-effect (and on the phase transformations) in pure samples were exclusively focused on the first order melting transition and the upper multicritical point B_{UMC}, above which the first order transition becomes a second order and the jump ΔM in the reversible magnetisation vanishes. On the other hand, transport and in particular specific heat measurements demonstrate the existence of a second lower multicritical point B_{LMC} along the vortex-melting line where again a first order melting transition is replaced by a second order transformation [13-14]. The existence of a crossover from the first-order to continuous transitions was also predicted by numerical simulations [15]. In most papers the value of this point was rather small, $B_{LMC} \approx 0.1T$.

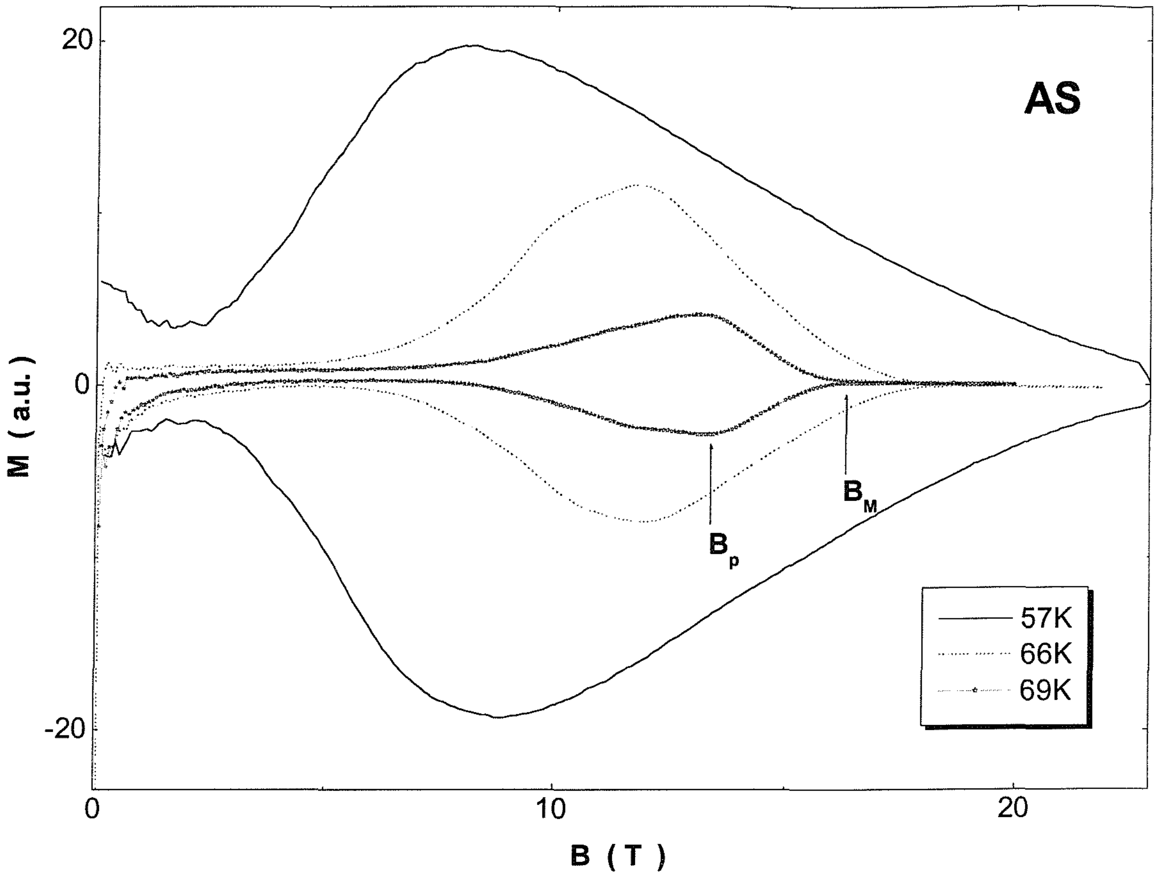

Fig. 4.1. Typical magnetisation curves showing the transformation to the conventional fishtail shape at low temperatures. Note that lowering the temperature enhances the signal. Arrows mark the characteristic field B_M and B_P.

Instead, Roulin et al. [16] using calorimetric techniques reported a very high value of B_{LMC}=5.25T in a high pressure fully oxidised twinned single crystal. This very high value might be related to the presence of twin planes that by acting as a source of pinning can deteriorate the periodicity of the vortex lattice at low fields. For this reason, here we have chosen to study several differently prepared twin-free YBCO single crystal in an oxygen state very close to y=7. Using the genesis of the peak-effect on the melting line $B_M(T)$, our aim is to clarify the existence and the value of this lower multicritical point and provide a description of the vortex-phase diagram near this point.

There are two other additional advantages in choosing an oxygen state in close proximity to y=7:

1. We know that the position of the low multicritical point is correlated to the presence of oxygen vacancies. In particular, with the fully oxidised state B_{LMC} reaches its highest value [16].
2. Y=7 means absence of oxygen vacancies which we have seen to be the main source of pinning in this system. Therefore, no such kind of pinning mechanism can be present near B_{LMC}, simplifying our analysis of data.

In Fig. 4.1 magnetisation curves M(B) obtained in the low temperature range are presented. The graph also illustrates how to determine the characteristic points: $B_P(T)$ defining the position of the peak and $B_M(T)$ defining the position of the melting point. As just discussed, these points define two different phase transitions which correspond respectively to destruction of the Bragg-glass phase and to melting of the vortex-solid. Note that in this range of temperatures the signal is very large and it increases with decreasing the temperature. Note also that with further decrease of T a conventional broad fishtail shape (with $B_M/B_P>2$) is produced as it is demonstrated for T=57K. This behaviour is common to most YBCO crystals and it exists down to the lowest measured temperature [17].

Fig. 4.2 shows the transformation of the magnetisation curves approaching the upper multicritical point (i.e. increasing the temperature). More exactly the peak in the (irreversible) magnetisation (given by the difference between lower and upper branch of the hysteresis loop in the figure) decreases its width and becomes extremely narrow.

The smallest width that we observed is in ZY sample. In this case the difference B_M-B_P reaches ~(1-2)% of the melting field B_M. This peak in the critical current has a width even smaller than in conventional superconductors [18] and disappears completely for B_{UMC}. This is a point of convergence of several phase lines separating vortex liquid, ordered Bragg glass and disordered solid states.

Fig. 4.3 summarises a typical behaviour of the magnetisation curves for the fully oxidised YBCO for all the wide temperature range studied. It clearly demonstrates the existence of three different regions related to the two multicritical points. The peak in the

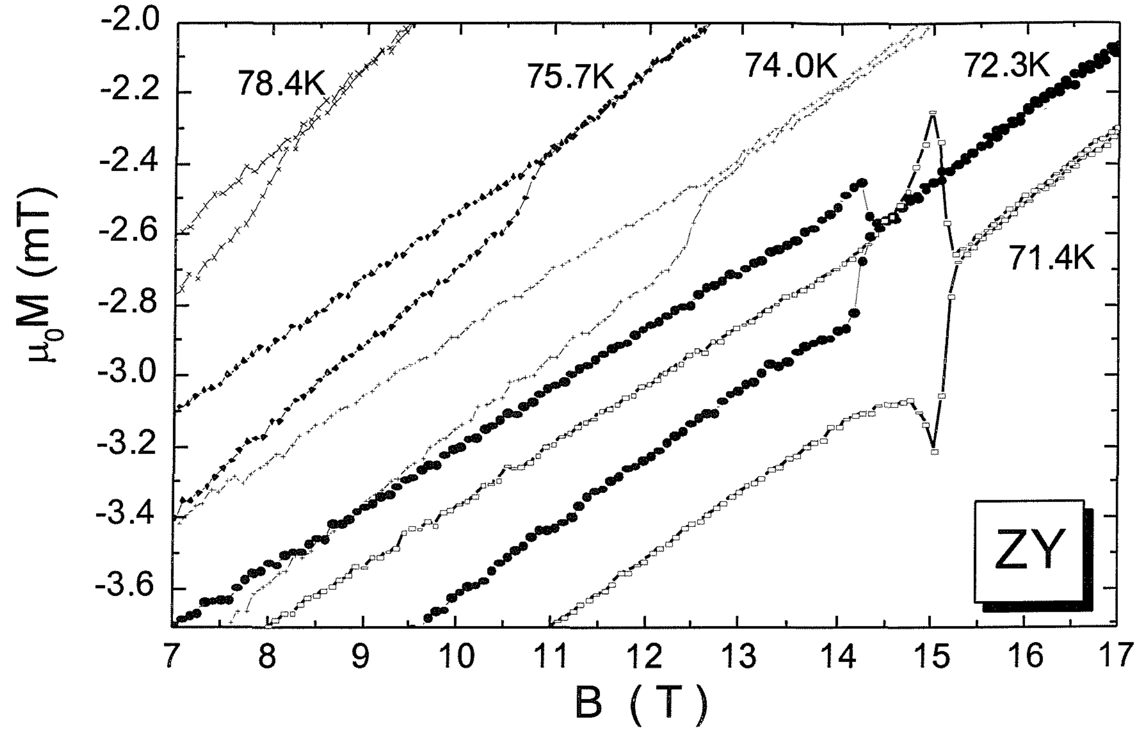

Fig. 4.2. Magnetisation curves for ZY sample at different temperatures approaching the upper multicritical point. Note the narrowness of the peak for T=71.4K and the irreversibility for T≥74K ($T>T_{UMC}$) present in the upper branches of the curves.

irreversible magnetisation characterises the region of low temperatures as has already been shown in Fig 4.2 and it is shown again in Fig. 4.3-a. At intermediate temperatures, when melting field falls between B_{UMC} and B_{LMC}, the curves M versus B are essentially reversible and we observe a jump ΔM that clearly identifies a first order transition. This jump is evident in Fig. 4.3-b. This means that in an intermediate temperature region it is an ordered solid phase (Bragg-glass) that melts and becomes liquid. For the crystal studied we have obtained two different types of behaviour in this range of temperature. Either with very small irreversibility or with irreversibility close to a jump value. In this case the jump essentially disappears on the return part (upper branch) of the magnetisation curve (see in fact Fig. 4.2 for T>74K). However this behaviour cannot be connected to the presence of a surface barrier. This explanation in fact predicts M≈0 for

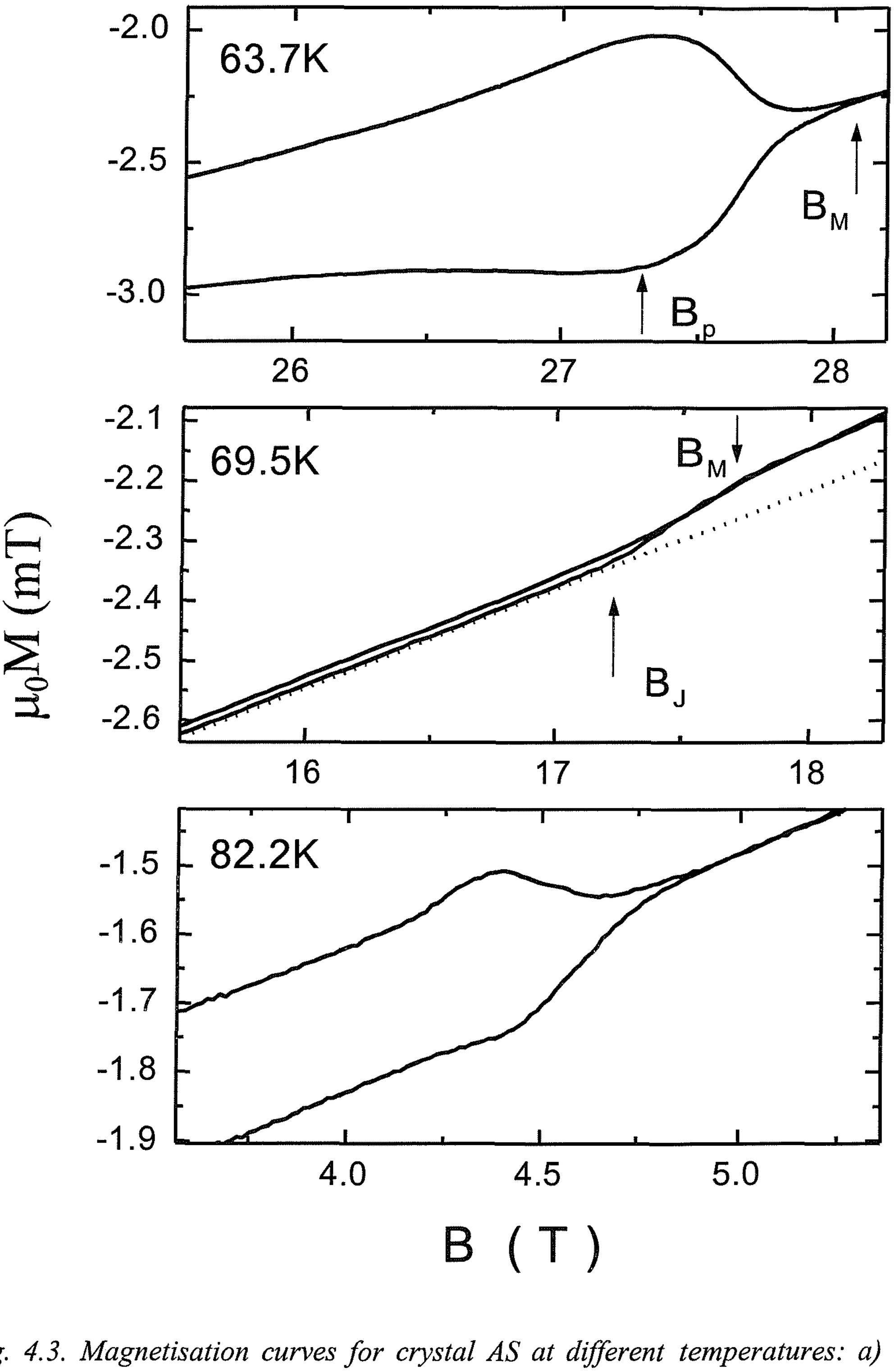

Fig. 4.3. Magnetisation curves for crystal AS at different temperatures: a) above the upper critical point b) between the two critical points and c) below the lower critical point B_{LMC}=5.5T. Dashed line in b) demonstrates the presence of the magnetisation jumps induced by first order melting transition at intermediate temperatures. Arrows mark the characteristic fields B_M, B_J and B_P.

the reverse part of the magnetisation curve. Furthermore when the sweep of the magnetic field is stopped the magnetic moment drops very fast and approaches an average point between ascending and descending branches of the loop. This result suggests that the irreversible part is essentially the same for both branches and also rejects a connection with the surface barrier. Note that two points are indicated in Fig. 4.3-b that characterise the melting transition: they are the field parameter B_J and B_M corresponding respectively to the onset and to the end of the jump. The finite width of the transition is related to sample inhomogeneities [19].

Fig. 4.3-a and b clearly demonstrate that the peak effect is connected to the first order transition jump in the reversible magnetisation. In fact, the peak is not only a precursor of the melting transition but the decreasing branch of the peak (B_M-B_P) essentially has the same width as the first-order jump.

Approaching higher temperatures the irreversible part of the loop increases drastically and we again obtain a very narrow peak-effect near $B_{LMC} \cong 5.5T$ (Fig. 4.3-c). The jump ΔM disappears completely: in this case a disordered solid (vortex-glass) melts and transforms in to a liquid via a second order transition. The presence of a narrow peak effect allows us to detect this second multicritical point. For the most studied crystal of this thesis (ZY) the two multicritical points are $B_{UMC} \cong (72K, 14.5T)$ and $B_{LMC} \cong (82K, 5.5T)$. It is interesting to note that although the value of the high multicritical field shows significantly high variations for different samples with identical oxygen content (14.5T, 19T and 22T for ZY, D3 and AS respectively), *the low multicritical point for all the studied samples has the same value* $B_{LMC} \approx 5.5T$. Therefore, it appears that B_{LMC} is not influenced by different preparation procedures but only by the oxygen content.

In order to demarcate the Bragg glass phase, we studied the biggest sample (ZY) near both multicritical points with the partial magnetisation loop technique [5-20]. With this measuring procedure, first the sample is cooled in zero field. Subsequently, in a series of consecutive runs while the temperature is kept constant, the field is swept up to a maximum value B_{max} and decreased back to zero. At each consecutive cycle B_{max} is gradually increased by a small quantity in order to reach and map values above the irreversibility field. As was shown theoretically [27] vortex-vortex interaction energy drops faster than pinning energy therefore increasing the field is equivalent to increasing disorder. The purpose of our partial loop experiment is to observe magnetic history effects that should characterise the creation of a highly disordered vortex phase, similarly to what happens in other disordered systems like spin glasses [21]. Therefore, by repeating the above described procedure for a series of different temperatures, it is possible to individuate in the plane B-T the transition between a dislocation-free system and a disordered phase.

We used a vibrating sample magnetometer for this kind of measurement for two reasons:

a) The partial magnetisation loop technique requires a very high temperature stability that cannot be obtained by the High Field Transport Arrangement in Grenoble.

b) The partial magnetisation loop technique requires very time-consuming measurements that are not compatible with the limited time available at the High Field Laboratory.

In Fig. 4.4 we show typical series of sweeps obtained at $T>T_{LMC}$ ($T>82K$). We observe that the partial loops coincide with each other until 0.15T. Until this point the history effects are not present due to the elastic structural properties of a Bragg glass. Then history dependencies start to appear and persist until 0.6T. These effects are probably induced by supercooling of a disordered phase and are generated by dislocations in the vortex-solid system. From the point in which they disappear a creation of a completely disordered phase is completed. At this point a saturation in the density of dislocations is reached and the disorder is not anymore influenced by the changing field. The difference between the magnetisation of consecutive loops is plotted in the inset of Fig. 4.4 and demonstrates a sharp onset of history effects above the point B_{pl} that is indicated by the arrow. This is the first time that such a behaviour has been reported below the lower multicritical point of YBCO.

It should be mentioned that for a significant temperature interval, in contrast to the behaviour near the upper multicritical field, near B_{LMC} a splitting of the peak effect is observed. This is also evident from Fig. 4.4 where two peaks are clearly discernible. Such splitting was first observed by K. Deligiannis et al. [22] and probably has its origin from the intermixture of different vortex states: liquid, disordered glass and Bragg glass phases [23-24]. We could speculate that as the first peak defines a transition from a mixture of different ordered solids to a completely disordered glass [23-25], this second peak marks a transition from a glass-liquid mixture to a complete liquid phase. The coexistence of liquid and vortex-solid, which produces an injection of a superheated ordered phase and a

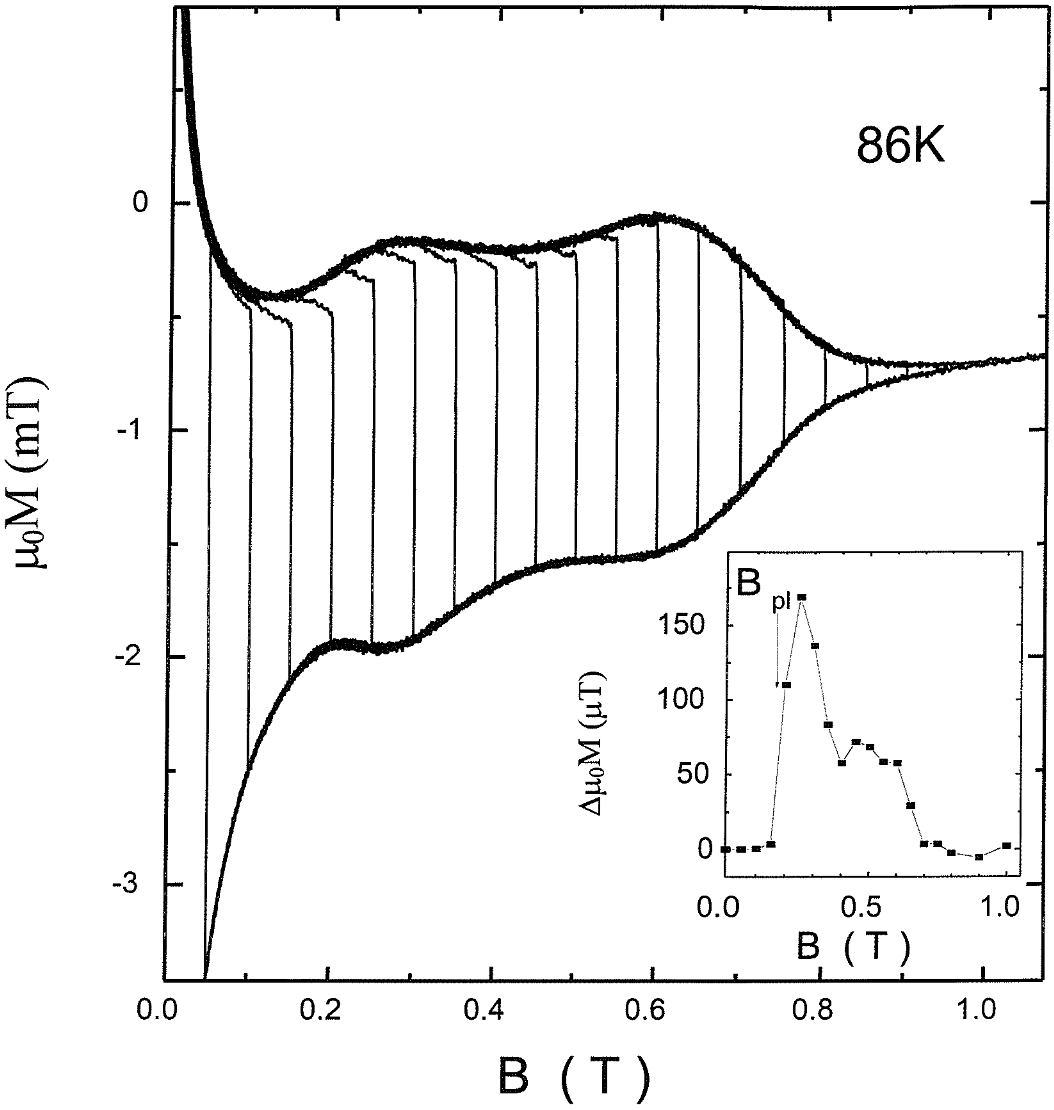

Fig. 4.4. Partial magnetisation loops for crystal ZY at $T=86K>T_{LMC}$. The inset shows the difference between consecutive partial loops. The arrow defines the onset of the history effects B_{pl}.

supercooled liquid phase in the region of the multicritical point is a probable reason for peak splitting. Of course, this particular and unusual feature requires further detailed investigations but it seems obvious to correlate this behaviour to a complicated intermixed phase.

It is also worth noting that the presence of this phase has already been observed either in calorimetric measurements [16] (where the peak in the specific heat related to a first order transition is followed by a step which only disappears completely by significantly increasing the magnetic field) and recently in BSSCO crystals using magneto-optical techniques [26]. In particular, the latter experiment has made it possible to directly resolve the melting process in a disordered superconductor, showing the presence of supercooled mesoscopic liquid domains induced by the presence of quenched disorder .

4.4 Phase Diagram and Multicritical Points in $YBa_2Cu_3O_7$

Using the characteristic fields, which are determined as shown in Fig. 4.1, 4.3 and 4.4 for different temperature ranges, we obtain a map of the phase diagram presented in Fig. 4.5. Here we have indicated two multicritical points on the melting line $B_M(T)$ and all different vortex-phases: Bragg-glass, mixture, vortex-glass, liquid. We also show the points representing the onset of the history effects $B_{PL}(T)$ collected with the VSM. As with the behaviour in the low temperature region [11], the line defined by these points coincides with the line defined by the onset of the peak-effect $B_{ON}(T)$. This provides a full demarcation of the Bragg glass phase. Note that the positions of both multicritical points is different from the positions estimated from the approximated intersections of $B_P(T)$ and $B_M(T)$ [22].

As can be seen, the behaviour of the peak effect is very symmetrical for both B_{UMC} and B_{LMC}, but what is really surprising is the shape of the phase diagram after normalisation of each point of the characteristic lines by the corresponding melting field value; see Fig. 4.6. This fact suggests a strong similarity in the genesis of the phenomenon of the peak-effect in both regions.

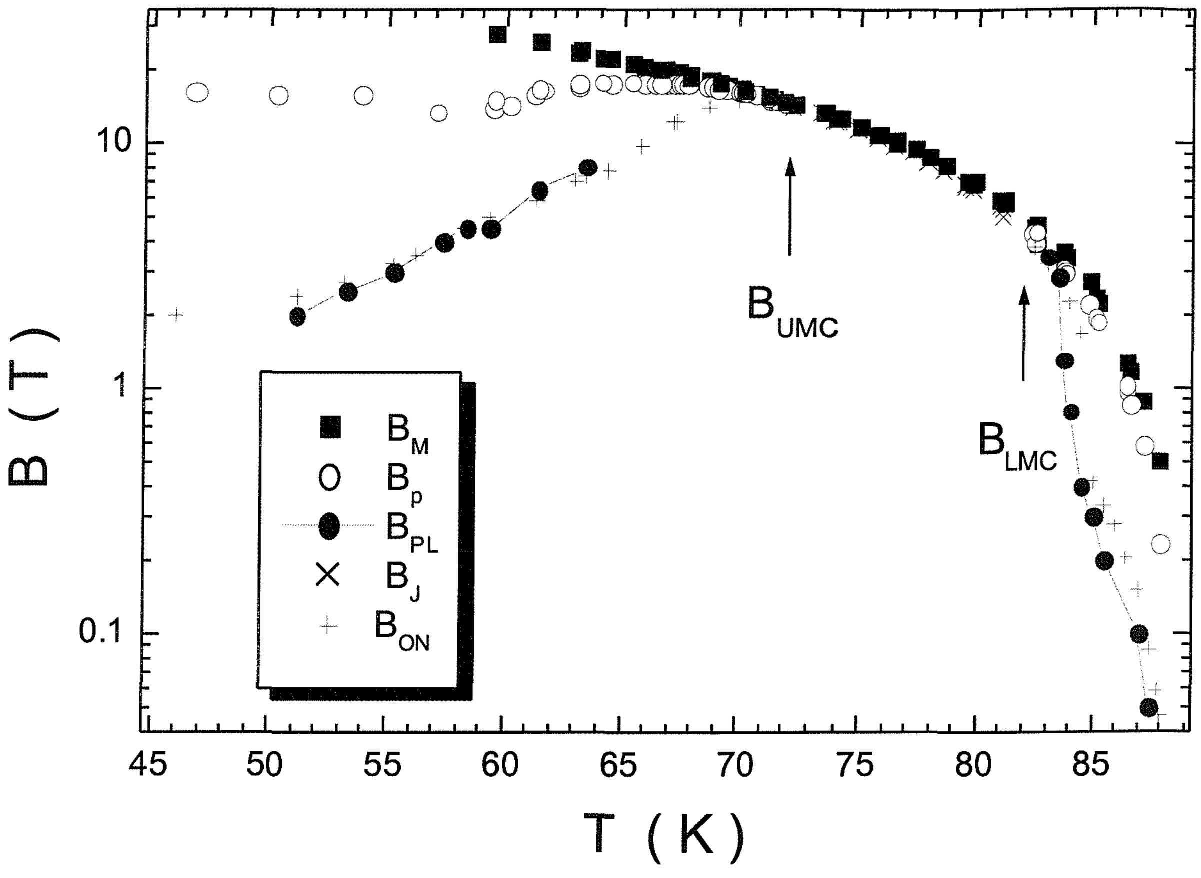

Fig 4.5. Phase diagram for crystal ZY. In the figure are represented the characteristic fields: melting transition B_M*, position of the peak* B_p *and of the onset of the peak effect* B_{ON}*, beginning of history effects* B_{PL}*, and finally position of the melting jump* B_J*. For the region of the first order transition* B_M *was determined by the end of the melting jump in the reversible magnetisation and outside this region* B_M *was related to the vanishing point of the irreversibility.*

We have already discussed one of the signatures of the melting phase transition: the jump of the reversible magnetisation ΔM in crossing the $B_M(T)$ line. The use of the Clausius-Clapeyron equation for a magnetic first-order transition shows the relation between ΔM and the change of entropy:

$$\Delta S = -\left(\frac{\Delta M}{B_M}\right)\left(\frac{dB_M}{dT}\right)\frac{\mathrm{d}\Phi_0}{K_B} \qquad (4.1)$$

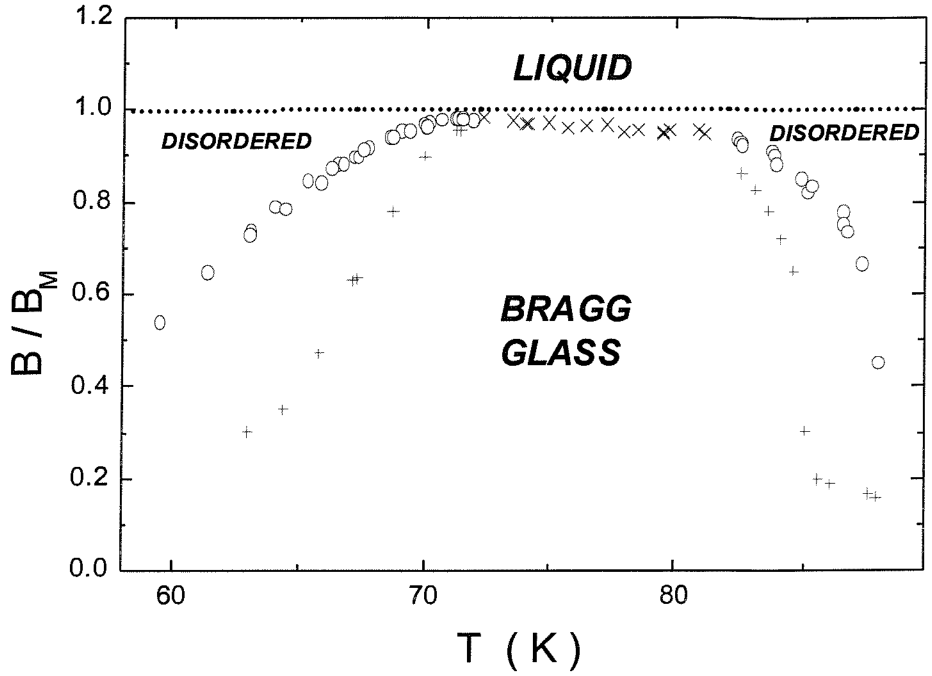

Fig. 4.6. Characteristic fields normalised by the melting field B_M. The different vortex phase regions are included in the figure. Symbols are the same as in Fig. 4.5.

where Φ_0 is the flux quantum, $d=11.7\times10^{-8}$cm is the c-axis lattice period, and K_B is the Boltzmann constant. This equation is valid along all the first-order melting line. In Fig. 4.7 we show the jump ΔM and the irreversible magnetisation at the peak $\Delta M_P \sim J_C$. We note that while the jump ΔM vanishes at both the multicritical points, ΔM_P starts to increase. Again, we notice a very pronounced symmetry below and above the corresponding two multicritical points.

The lower multicritical point was probably observed for the first time by U. Welp et al. [13] in 1996. Using transport and SQUID magnetometry techniques, they demonstrated coincidence of discontinuous jumps in magnetisation with resistive drops in the H-T plane confirming the existence of a first order melting transition of the flux lattice in untwinned YBCO crystals. They observed disappearance of this first order transition (that means the disappearance of the jumps, i.e. $\Delta M=0$ and $\Delta S=0$) at about 90K well below the zero-field transition temperature. This behaviour was attributed to the residual sample inhomogeneity which becomes more important approaching the transition temperature T_c. They thought that, decreasing the number of vortices with decreasing the field, residual pinning centres might become more important and dominate in the high temperature–low field region of the phase diagram.

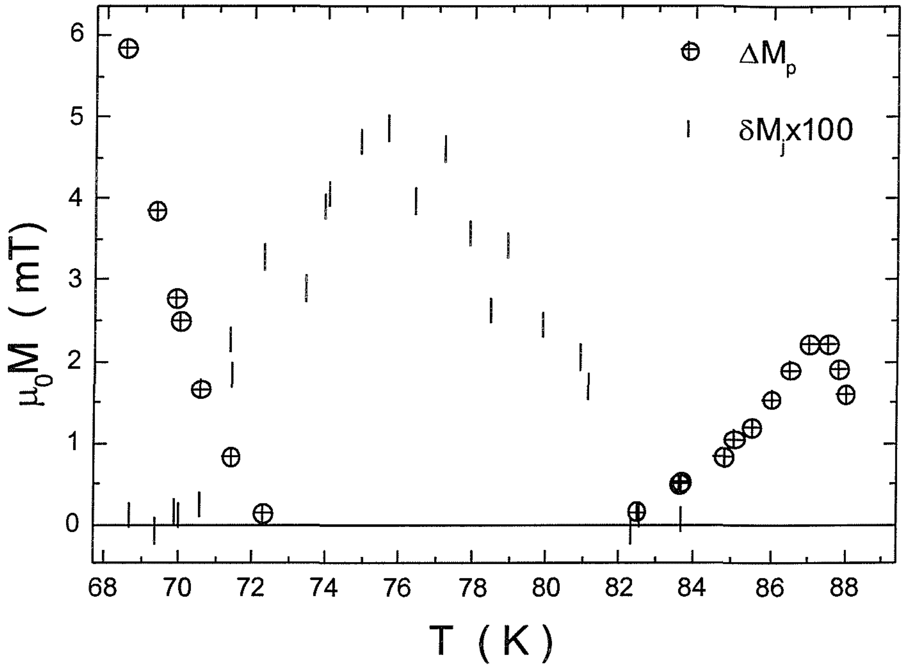

Fig. 4.7. Temperature dependence of the melting jump value in reversible magnetisation δM_J and of the irreversible magnetisation at the peak ΔM_P for crystal ZY.

Our results do not support this interpretation. In fact, even in sample D3, that was annealed for a shorter time and therefore it was the most inhomogeneous (with a superconducting transition width 3 times larger than in the other two samples), the value of the lower multicritical point was always the same.

Following the phenomenological model of V. Vinokur et al. [27] it is not difficult to explain the transitions between different vortex-phases and the nature of the upper multicritical point B_{UMC}. There are three energies involved in this analysis: the vortex-vortex (or elastic) interaction $\mathbf{E}_{EL}$, the pinning interaction $\mathbf{E}_P$ (caused by randomly distributed material defects), and the thermal energy K_BT. Using the Lindemann criterion for the melting transitions all the boundary lines in the phase diagram can be obtained by balancing such characteristic energies. The vortex-vortex interactions are accounted for by a sort of "cage potential" that each vortex feels and that is due to neighbouring vortices perturbed by point disorder. A representative vortex is confined in a cage of transverse size $a_0 \sim B^{-1/2}$ (which is the nearest neighbour distance of the vortex-lines defined in chapter 1). The longitudinal size of this elastic cage is $L_0=2\varepsilon a_0$. It can be shown that:

$$\mathbf{E}_{EL}=\varepsilon\varepsilon_0 u^2/a_0 \tag{4.2}$$

where u is the vortex displacement, ε is the anisotropy parameter and $\varepsilon_0=\Phi^2{}_0/(4\pi\lambda)^2$ is the internal vortex energy per unit length. Applying the Lindemann criterion near the solid-solid transition, $\mathbf{E}_{EL}$ becomes:

$$\mathbf{E}_{EL}=\varepsilon\varepsilon_0 c^2{}_L a_0 \sim B^{-1/2} \tag{4.3}$$

with $c_L \sim 0.1\text{-}0.2$. Instead, for the pinning energy Vinokur et al. obtain:

$$\mathbf{E}_P=\pi(\gamma s)^{1/2}(L_0/s)^{1/5} \sim B^{-1/10} \tag{4.4}$$

Where s is the interlayer spacing and γ is the variance of the strength of point disorder.

Both $\mathbf{E}_{EL}$ and $\mathbf{E}_P$ decrease with the magnetic field and fall below K_BT at the melting field. But from 4.3 and 4.4 we see that, for a fixed temperature, when enhancing the magnetic field, vortex-vortex energy drops faster than the pinning energy. Therefore, it is stronger at low fields where, in fact, the vortex solid is an ordered Bragg glass. At higher fields the pinning energy dominates and produces a phase transition to a glass that has completely lost its translational order. Quenched disorder has thus induced lateral displacements distorting the cages and breaking the Bragg glass configuration. Further increasing the field causes a decrease of the pinning energy and when it is equal to the thermal energy K_BT a transition to a vortex-liquid state is produced. At the upper multicritical point all this three energies are equal. The data near B_{UMC} that we have shown are a further proof of the correctness of this description.

It is interesting to note that the same theory can be used to predict a lower multicritical point. In this case the vortex-vortex interaction does not grow anymore but instead drops exponentially. For this reason, we expect (after a Bragg-glass state) the appearance of a disordered lattice due the increased importance of the pinning energy and then again a melting to a liquid, like in the previous situation. However this should only happen at low field far below our experimental value of the lower multicritical point.

Another hypothesis that has been used to explain the nature of B_{LMC} is the re-entrant melting line. This phenomenon could be generated by: a) entropic factor [28], b) the exponential suppression of the vortex–vortex interaction in the case in which the inter-vortex spacing a_0 becomes smaller than the penetration depth λ [29]. However in both cases the value of B for this transition should correspond to fields smaller than $\mu_0 H_{C1}$. This is completely in contrast with our high value $B \approx 5T$.

It was shown recently that the presence of strong sources of defects can deteriorate the periodicity of the vortex lattice and originate the appearance of the lower multicritical point. In this case a strong pinning interaction $\mathbf{E}_{SP}$ should be able to destroy the ordered phase when it is bigger than the vortex-vortex interaction and should decay faster at the multicritical point. For V. Vinokur et al. [27] $E_{SP} \approx \varepsilon_0 n V_C$, where ε_0 is a pinning energy for one strong centre, n is the density of the centres and $V_C \approx a_0^{3/2}$ is the volume of a “cage”. Because its energy drops faster than the elastic energy they become equal at B_{LMC}. This mechanism can explain the existence of a disordered phase below the lower multicritical point and transition to a Bragg glass in columnar irradiated samples [14].

However this explanation cannot be used to interpret our results. The fact that all three samples were detwinned excludes the presence of strong pinning centres. Furthermore it is important to stress that not only all our samples have similar values of the lower multicritical point but also previous calorimetric measurements [16] performed on a fully oxidised YBCO crystal obtained almost the same value. They obtained the same value even after detwinning their specimens and this is exactly what we see in our AS and D3 samples which were detwinned as well. In addition, other very recent magnetic measurements have given a similar value $B_{LMC} \approx 5T$ [30]. All these facts suggest that B_{LMC} is rather independent of the sample quality. For this reason, we can exclude relevance of other extrinsic defects because is very unlikely to have the same defects concentration in differently prepared samples. The presence of oxygen clusters is also unlikely to explain the origin of the lower multicritical point. These clusters can be a source of a weak pining only and their concentration should drop approaching the fully oxidised state when all vacancies disappear. We have in fact verified that the value of

B_{LMC} increases with the decrease of the oxygen deficiency: in crystal AS $B_{LMC} \approx 0T$ for y=6.94 and increases to 5.5T for y=7 that is the fully oxidised state.

It is also worth mentioning that these results disagree with numerical simulations performed by Kienappel and Moore [31] which predict termination of the first order line and existence of a low end point. According to their analysis the first order line and the end point should exist for any oxygen content and this is in contrast with our experimental results.

Therefore we need to find another source of disorder with an intrinsic origin, whose importance becomes stronger approaching the fully oxidised state. We think that this source may come from the exotic nature of superconductivity of HTS. It is well known that the pseudogap is a common property of the cuprate materials. The pseudogap [32] is probably connected with the charge or spin density waves gap. Increasing the oxygen content should decrease the pseudogap value favouring spin/charge excitation. Therefore for sufficiently high temperatures there could be the possibility of the excitation of spin/charge disordered states which influence the behaviour of vortices leading to the appearance of the lower multicritical point. On the other hand B_{LMC} vanishes approaching the optimally doped state because the pseudogap value exceeds our temperature range limited by T_C. In our samples we observed the lower multicritical point for oxygen contents above 6.96. This idea is obviously speculative and certainly requires further analysis and comparative studies of the pseudogap properties and the multicritical point in HTS.

4.5 Summary and Conclusions

In summary, in this chapter we have shown magnetisation measurements performed on $YBa_2Cu_3O_7$ (fully oxidised) single crystals using a sensitive magnetic torque rig and a vibrating sample magnetometer. Our study of the genesis of the peak effect from the melting line allowed us to determine the characteristic fields, to demarcate different vortex-phases and to map the phase diagram up to 28 Tesla. In particular we have confirmed the unequivocal existence of the lower multicritical point along the melting line $B_M(T)$.

This point of convergence of several boundary lines, is located at low field (≈5.5T) and delimits (together with the upper multicritical point) the region in which an ordered vortex solid melts into a liquid via a first order transition. Close to both multicritical points we observed a very narrow peak effect with a width even smaller than in conventional superconductors. It is interesting to note that near the lower multicritical point we observe a splitting of the peak effect (the splitting exists near B_{UMC} as well but for oxygen content below 7 [22]). This phenomenon has been related to the intermixture of various vortex phases: Bragg glass, vortex glass and vortex liquid. Using the partial magnetisation loop technique the existence of history effects near both multicritical points was demonstrated providing a full demarcation of the part of the phase diagram occupied by the ordered Bragg-glass.

The behaviour of the boundary lines, the values of irreversible magnetisation and of the jump ΔM reveal a very pronounced symmetry. But the most impressive symmetry is observed in the phase diagram of Fig. 4.5 that is the most intriguing result of this chapter. The normalisation of the values of the boundary lines to the respective values of the melting field shows an almost perfect symmetry defined by the two multicritical points. The existence of the upper multicritical point can be explained in the framework of current existing theories. In a simple approach it should correspond to a point of equilibrium for different interaction energies: elastic, pinning and thermal. The phase diagram obtained by our measurements is consistent with such a scenario.

Instead, the nature and the origin of the lower multicritical point is not clearly understood yet. In this work we have demonstrated the intrinsic nature of B_{LMC}. In fact, the different preparation procedures strongly influenced B_{UMC} (different for different samples) but not B_{LMC}, almost the same for all studied samples. Furthermore this value is consistent with previous calorimetric measurements performed by Roulin et al [16]. These facts suggest a relation of the lower multicritical point to an intrinsic origin of disorder. We suggest the HTS pseudogap, that drops below T_C in overdoped crystals of YBCO, as a possible mechanism for lower multicritical point. It has to be noted that this idea is only speculative and other experiments have to be done to confirm our hypothesis.

References

1 A. Pippard, Phil. Mag. **19**, 217 (1969).

2 A. I. Larkin et al., J. Low Temp. Phys. **34**, 409 (1979).

3 S. Bhattacharya et al., Phys. Rev. Lett. **70**, 2617 (1993).

4 W. K. Kwok et al., Phys. Rev. Lett. **73,** 2614 (1994).

5 P. L. Gammel et al., Phys. Rev. Lett. **80**, 833 (1998).

6 Y. Paltiel et al., Phys. Rev. Lett. **85**, 3712 (2000); J. Kierfield and V. Vinokur, Phys. Rev. B **61**, 14928 (2000).

7 F. Hellmann et al., Phys. Rev. Lett. **68**, 867 (1992).

8 Th. Wolf et al. J. Cryst. Growth **96,** 1010 (1989). R. Gagnon et al., J. Cryst. Growth **121**, 559 (1992); H. Asaoka et al., Jpn J. Appl. **32**, 1091 (1993).

9 M. Oussena et al., Phys. Rev. Lett. **72**, 3606 (1994); S. N. Gordeev et al., Nature (London) **385**, 324 (1997).

10 D. J. L. Hong and D. M. Smith, J. Am. Ceram. Soc. **74**, 1751 (1991).

11 S. Kokkaliaris et al., Phys. Rev. Lett. **82**, 5116 (1999).

12 X. Ling and J. I. Budnick, in Magnetic Susceptibility of Superconductors and Other Spin Systems, edited by R. A. Hein, T.L. Francavilla and D. H. Liebenderg (Plenum, New York,1991) p. 377.

13 U. Welp et al., Phys Rev. Lett. **76**, 4809 (1996).

14 W. K. Kwok et al., Phys. Rev. Lett. **84**, 3706 (2000).

15 S. Ryu et al., Phys. Rev. Lett., **78**, 4629 (1997).

16 M. Roulin et al., Phys. Rev. Lett., **80**, 1722 (1998).

17 L.F. Cohen and H. J. Jensen, Rep. Prog. Phys. B **60**, 1581 (1997).

18 R. Meier-Hirmer et al., Phys. Rev. B **31**, 183 (1985), R.Wordenweber and P. Kes, Phys Rev. B **34**, 494 (1986); S. Bhattacharya and M. Higgins, Phys. Rev. Lett. **70** 2617 (1993); S. S. Banerjee et al., Phys. Rev. B **58**, 995 (1998).

19 E. Zeldov et al., Nature (London) **375**, 373 (1995).

20 S. B. Roy and P. Chaddah, J. Phys.: Condens. Matter **9**, L 625 (1997).

21 J. A. Mydosh, Spin Glasses: An Experimental Introduction (Taylor and Francis, London, 1993).
22 K. Deligiannis et al., Phys. Rev. Lett. **79**, 2121 (1997).
23 A. A. Zhukov et al., Phys. Rev. B **61**, 886 (2000).
24 A. P. Rassau et al., J. Low Temp. Phys. **117**, 1507 (1999).
25 Y. Paltiel et al., Nature **403**, 398 (2000).
26 A. Soibel et al., Nature **406**, 282 (2000).
27 V. Vinokur et al., Physica C **295,** 209 (1998).
28 D. R. Nelson, Phys. Rev. Lett. **60**, 1973 (1998).
29 J. Kierfeld. Physica C **300**, 171 (1998).
30 T. Nishizaki et al. , will be published in Physica C.
31 A. K. Kienappel and M. A. Moore cond-mat/9804314.
32 T. Timunsk and B. Statt., Rep. Prog. Phys., **62**, 61 (1999).

Pages 72-93
(Chapter 5)
missing from
this Thesis

Main Conclusions

In this thesis we performed magnetic measurements on three fully oxidised (i.e. y=7) single crystals of $YBa_2Cu_3O_y$ and transport measurements on a single crystal of 2H-$NbSe_2$ with low concentration of impurity ($J_C/J_0 \approx 10^{-3}$). The aim of this work was to elucidate the phase diagram and behaviour of the melting line for both materials.

In particular with regard to $YBa_2Cu_3O_7$, using a highly sensitive magnetic torque rig and a vibrating sample magnetometer for the study of the genesis of the peak effect from the melting transition, we have determined the characteristic fields, demarcated the different vortex-phases and mapped the phase diagram up to 28 tesla. The unequivocal existence of the lower multicritical point along the melting line $B_M(T)$ was confirmed. This point of convergence of several boundary lines, is located at low field (≈5.5T) and defines (together with the upper multicritical point) a region in which an ordered vortex solid melts into liquid via a first order transition. Close to these two points we observed a very narrow peak with a width even smaller than observed in conventional superconductors. We demonstrated the existence of history effects near both multicritical points and defined the space occupied in the B-T plane by the ordered Bragg-glass phase.

The behaviour of the boundary lines, the values of irreversible magnetisation and of the jump ΔM reveal a very pronounced symmetry. But the most impressive symmetry is observed in the phase diagram of Fig. 4.6. The normalisation of the values of the boundary lines to the respective values of the melting field shows a quite pronounced symmetry defined by the two multicritical points. The existence of the upper multicritical point can be explained in the framework of current existing theories. Instead, the nature and the origin of the lower multicritical point is not yet clearly understood. With this work we have demonstrated the intrinsic nature of B_{LMC}. In fact, despite considerable differences in the values of the upper multicritical point, almost the same value of the lower multicritical point was obtained for all samples with the same oxygen content and different preparation procedures. Furthermore this value is consistent with previous calorimetric measurements. These facts may correlate the lower multicritical point with an intrinsic origin of disorder. We suggest that B_{LMC} is connected with the HTS pseudogap that in overdoped YBCO falls below T_C.

The other system that is investigated in this work is the low T_C superconductor 2H-$NbSe_2$, widely studied in recent years due to its weak pinning properties and significant role of anisotropy and thermal disorder. A ^3He system allowed us to perform transport measurements using the standard dc four probe technique down to 0.3 Kelvin. We measured the resistance of the sample as a function of the temperature (for fixed magnetic fields) and of the magnetic field (for fixed temperatures). Different driving currents were used. From these measurements we have extracted the upper critical field $B_{C2}(T)$ and elucidated details of the thermal melting transition of the vortex-solid. Combing our data with magnetic measurements performed on a similar sample we obtained a demarcation of the different vortex phases and a complete description of the phase diagram of this material.

All the resistive curves obtained either by varying the temperature or the magnetic field show an abrupt drop which was interpreted as a small region of the phase diagram connected to the melting process of the vortex-solid. It is worthwhile noting that this melting region does not approach the upper critical field $B_{C2}(T)$ when reaching very low temperatures (0.3 Kelvin) as the theory predicts. To the best of our knowledge this is the first time that such behaviour has been observed in a superconductor.

We have found a good agreement between our transport measurements and the data measured on a similar sample using magnetic techniques [Ref. 12 chapter 5]. In fact the irreversibility line extracted by the latter measurements almost coincides with our melting region.

One of the most interesting features displayed by 2H-$NbSe_2$ is a very narrow jump (T_J) observed in the final part of the melting transition by the resistance versus temperature (or field) curves: this resistive anomaly develops in less than one millikelvin. The possibility of a first order transition probably may be excluded. The fact that this part of the resistive curves (and only this part) shows a hysteretic behaviour and that the position of this sharp tail depends slightly on the driving current, suggests that the origin of this surprising and unusual phenomenon is a strong depinning process.

Both YBCO and $NbSe_2$ belong to the wide class of type II superconductors. The work presented here allowed us to compare the vortex phase diagrams of both materials and it is evident that there are some similarities and substantial differences. As it is stressed in chapter 5 the most important difference is probably the absence of a first order solid-liquid transition in $NbSe_2$. Here, the transformation of the Bragg glass in a complete amorphous phase is observed at all temperatures $T<Tc(0)$. Instead, it is exactly the presence of a thermodynamic first order transformation that in YBCO produces a so complicated phase diagram and the presence of multicritical points.

For the cuprates, properties such as anisotropy, intrinsic layering, large penetration depths and small coherence lengths amplify the effects of thermal fluctuations. For this reason flux-liquid that is a disordered phase occupies a large portion of the phase diagram and the Ginzburg number G_i is large compared to the conventional low T_C cousins. In $NbSe_2$ the effects of thermal fluctuations are enhanced for reason similar to those in HTS and G_i is relatively large in respect to low T_c materials but nevertheless small when compared to materials like YBCO. On one hand this explains why it is possible to explore regimes, phases and phases transitions already seen in the context of HTS but on the other hand is also the reason for the above described substantial difference.